



HAL
open science

Brittle fracture mechanisms and toughness of model low alloy steels chemically representative of macrosegregated forgings

Caina Bemfica de Barros, Ludovic Vincent, Bernard Marini, Jean-Philippe Mathieu, Daniel Brimbil

► To cite this version:

Caina Bemfica de Barros, Ludovic Vincent, Bernard Marini, Jean-Philippe Mathieu, Daniel Brimbil. Brittle fracture mechanisms and toughness of model low alloy steels chemically representative of macrosegregated forgings. *Journal of Nuclear Materials*, 2025, 607, pp.155668. 10.1016/j.jnucmat.2025.155668 . cea-04939329

HAL Id: cea-04939329

<https://cea.hal.science/cea-04939329v1>

Submitted on 10 Feb 2025

HAL is a multi-disciplinary open access archive for the deposit and dissemination of scientific research documents, whether they are published or not. The documents may come from teaching and research institutions in France or abroad, or from public or private research centers.

L'archive ouverte pluridisciplinaire **HAL**, est destinée au dépôt et à la diffusion de documents scientifiques de niveau recherche, publiés ou non, émanant des établissements d'enseignement et de recherche français ou étrangers, des laboratoires publics ou privés.



Distributed under a Creative Commons Attribution 4.0 International License



Brittle fracture mechanisms and toughness of model low alloy steels chemically representative of macrosegregated forgings

Cainã Bemfica^a, Ludovic Vincent^{a,*}, Bernard Marini^a, Jean-Philippe Mathieu^b, Daniel Brimbal^c

^a Université Paris-Saclay, CEA, Service de Recherche en Matériaux et procédés Avancés, 91191, Gif-sur-Yvette, France

^b EDF Lab Les Renardières, Dpt. MMC, 77250 Moret-Loing-et-Orvanne, France

^c Framatome SAS, Direction Technique et Ingénierie, 92400, Courbevoie, France

HIGHLIGHTS

- Model low alloy forged and tempered steels have been manufactured with chemical compositions representative of RPV steel at nominal composition, high and very high levels of macrosegregations.
- Contrary to what is observed on common carbon steels, the lowest fracture and impact toughness transition temperatures are obtained for the highest carbon content alloy.
- Intergranular fracture is observed for the most enriched and brittle resistant model material.
- Cleavage fracture is observed on the nominal and high carbon content materials, initiating from molybdenum/manganese enriched carbides located at grain boundaries.
- The improvement of brittle fracture resistance with the level of carbon content is analyzed as the combined result of a higher hardenability of the material, that produces a smaller grain size and tougher crystalline microstructure, and of a smaller size of the carbides in the material.

ARTICLE INFO

Keywords:

RPV steel
Macrosegregation
Brittle fracture
Fracture toughness

ABSTRACT

The influence of the chemical composition on the brittle fracture behaviour of quenched and tempered low alloy bainitic steels was investigated thanks to the laboratory elaboration of three model alloys which have undergone a heat treatment to improve their chemical homogeneity. Two model materials with chemical compositions simulating zones of large (0.29 %C) and intense (0.38 %C) positive macrosegregation were characterized and compared with the nominal composition material (0.18 %C). The ductile to brittle transition temperatures T_{56J} and T_0 of the materials with nominal and large carbon content are similar, whilst those of the material with the highest carbon content are unexpectedly significantly lower. Fractographic analyses indicate that the brittle fracture mechanisms depend also on the chemical composition. For 0.18 and 0.29 %C, cleavage is the dominant brittle fracture mechanism, whilst a mix of cleavage and intergranular failure is observed for 0.38 %C at the same levels of fracture energy or toughness. When cleavage failure is the dominant mechanism, it often originates at large molybdenum and manganese-enriched carbides located at grain boundaries likely identified as former austenitic grain ones. Microstructural analyses show variations of the large carbide population and ferritic grain size between the three alloys. Also, as carbon content increases, an evolution towards a lower bainite/martensite crystallographic microstructure is observed. The effects of these microstructural differences on the brittle fracture behavior are discussed.

1. Introduction

In the nuclear industry, parts of very large components such as the

Reactor Pressure Vessel (RPV), the pressurizer and the steam generator are forged from heavy ingots. These ingots generally contain zones of positive macrosegregation, where the content of carbon, other alloying

* Corresponding author.

E-mail address: ludovic.vincent@cea.fr (L. Vincent).

<https://doi.org/10.1016/j.jnucmat.2025.155668>

Received 3 November 2024; Received in revised form 27 January 2025; Accepted 29 January 2025

Available online 30 January 2025

0022-3115/© 2025 The Author(s). Published by Elsevier B.V. This is an open access article under the CC BY license (<http://creativecommons.org/licenses/by/4.0/>).

elements and impurities is larger than the nominal composition of the ingot. Positive macrosegregation has an industrial impact because it may lead to the embrittlement of ferritic steels such as RPV steels [1–6]. For some large forgings, macrosegregated zones cannot be fully eliminated during fabrication and limited segregations can still be present in the final component. In some rare cases where the level of macrosegregation could be larger than expected, extensive destructive material characterizations can be required to check that the brittle fracture toughness still ensures the structural integrity of the component [5,6].

The microstructure of macrosegregated materials can feature some important differences when compared to non-segregated materials. As expected, it was observed that carbide and inclusion density increased due to the macrosegregation [7–9], which has been appointed as the main cause for possible embrittlement [7,10,11]. However, in addition to the bulk chemical composition enrichment associated with macrosegregation, local zones of microsegregation originated during the ingot casting are much more abundant and intense in the macrosegregated zones than in the non-macrosegreated ones [3,7,9,10,12]. Consequently for a given cooling rate, several heterogeneous microstructures such as upper bainite, lower bainite, martensite and martensite-austenite (M-A) islands have been reported for the same macrosegregated samples [3,7–10] after quenching phase of the processing route, not considering post-forging & welding heat treatments. Due to these microstructural and chemical heterogeneities, it is not straightforward to isolate the effects of the bulk chemical composition on brittle failure. For instance, Yan and co-workers [10] observed, for the same bulk chemical composition, an increase of almost 60 J on the average absorbed energy from Charpy tests at $-21\text{ }^{\circ}\text{C}$ after a homogenization heat treatment. This result was attributed to the reduction of the M-A island's content, which were detrimental to the toughness properties since they decomposed into ferrite and carbide-rich zones after tempering. Within this context, an investigation of the effects of bulk chemical composition evolution (i.e. macrosegregation without microsegregation) on the brittle failure of low alloy steel large forgings is of interest. For this purpose, tensile tests, Charpy V-Notch impact tests and brittle fracture toughness tests were performed on three model materials manufactured with different levels of carbon content and the corresponding co-segregated alloy elements. These alloys had been submitted to a homogenization heat treatment prior to forging and classical heat treatments performed on industrial components, in order to reduce drastically microsegregations. The microstructures of the alloys are investigated as well as the nature of the brittle fracture initiators when relevant. Finally, an empirical approach and a local approach model to brittle fracture are used to study the variation of the cleavage critical stress between the three materials.

2. Materials and experimental methods

2.1. Materials

Three materials obtained from small laboratory castings ($\sim 100\text{ kg}$, with $\sim 55\text{ kg}$ that remain after ingot head cutting) have been investigated: a material with a chemical composition similar to the RCC-M code material type 18MND5 bainitic pressure vessel steel (close to ASME A508 Gr3 Cl2)—i.e. non-segregated material—and two materials with chemical compositions simulating zones of large ($\sim 0.29\text{ \%C}$) and intense ($\sim 0.38\text{ \%C}$) positive macrosegregation. Table 1 presents the chemical compositions of the three model materials. As can be seen, for

the two materials simulating positive macrosegregations, the content of other elements such as Mn, Ni, Mo are also increased compared to the 18MND5 type composition, thus reproducing the typical chemical composition observed in macrosegregated zones of large forgings. However, for the sake of simplicity, in the following, each material will be referred to by its carbon content and property variations between the model alloys will be mainly discussed based on the carbon content variation.

For all materials, a homogenization heat treatment ($1200\text{ }^{\circ}\text{C}$, 24h) was carried out before forging operations in order to reduce as much as possible the microsegregations that could be observed notably for materials simulating the highest level of macrosegregation in a previous investigation [8,9]. Although this homogenization treatment is not exactly the treatment performed at the heating of the ingot on industrial components, it was carried out on the current laboratory materials in order to try to separate the effects of the “bulk chemical composition” from those of the micro-segregations. After homogenization, forging operations were carried out in two phases, leading to an equivalent forging ratio of ~ 4.65 . Forging is followed by a heat treatment procedure, which consists of baking, austenisation, quenching and tempering, and post-weld heat treatments (see Fig. 1 for temperatures and durations).

To assess the effectiveness of homogenization, Vickers microhardness HV0.2 maps (60 vs 60, indentations separated by $150\text{ }\mu\text{m}$) were obtained. When compared to the previous experimental work [8,9], the average hardness is similar, but a reduction in the standard deviation is observed for all materials, especially for the highest carbon content, that was also the most microsegregated in the previous work: at $\sim 0.18\text{ \%C}$, a reduction from 13 to 7 HV was observed; at $\sim 0.29\text{ \%C}$, from 18 to 11 HV; and at 0.38 \%C , from 21 to 7 HV.

2.2. Mechanical tests

Mechanical characterization was carried out using both tensile and fracture mechanics tests. Tensile tests were conducted according to the NF EN ISO 6892 standard Sections 1 and 3 depending on the test temperature. Testing was made on a MTS rig, with a 100kN loading cell. Closed loop control consists in a constant beam displacement at 0.6 mm/min , leading to an estimated equivalent strain rate of 2.10^{-4} s^{-1} . To characterize the brittle failure resistance of the three materials, impact tests on standard Charpy V-Notched (CVN) specimens and fracture toughness tests on 12.5 mm thick Compact-Tension (CT) specimens were carried out. CVN tests were conducted according to the NF EN ISO 148–1 standard, on a Brugger RKP 450J pendulum striker from Zwick-Roell, equipped with an automated system that ensures both thermal regulation and automatic transfer of the test specimen to the anvil. CT toughness measurement tests were done according to the ASTM E 1921 standard on a MTS rig with a 100kN loading cell. For Charpy tests, between 2 and 4 tests were performed at each temperature. For 0.18 %C and 0.29 %C grades, tests were carried out at 8 different temperatures, whilst 9 temperatures were used for the 0.38 %C one. In total, 20 specimens were used for each material. The investigated temperatures ranged from $-140\text{ }^{\circ}\text{C}$ to $150\text{ }^{\circ}\text{C}$, resulting in energy levels between 5 and 218 J. For fracture toughness tests, between 2 and 5 tests were carried out at each temperature. For 0.18 %C and 0.29 %C, tests were carried out at 4 different temperatures, whilst 5 temperatures were used for 0.38 %C. In total, 15 specimens were used for each material. The investigated temperatures ranged from -150 and $+30\text{ }^{\circ}\text{C}$, resulting in fracture

Table 1
Chemical compositions (in % wt) of the three model materials. Fe as balance.

Material	C	Mn	Ni	Mo	Cr	Si	Al	O	N	P	S
0.18 %C	0.18	1.47	0.76	0.50	0.17	0.18	0.013	0.0021	0.0023	0.0077	0.0012
0.29 %C	0.29	1.67	0.83	0.58	0.17	0.23	0.0259	0.0017	0.002	0.0074	0.0024
0.38 %C	0.38	1.79	0.90	0.64	0.17	0.26	0.0257	0.0016	0.0021	0.0074	0.0023

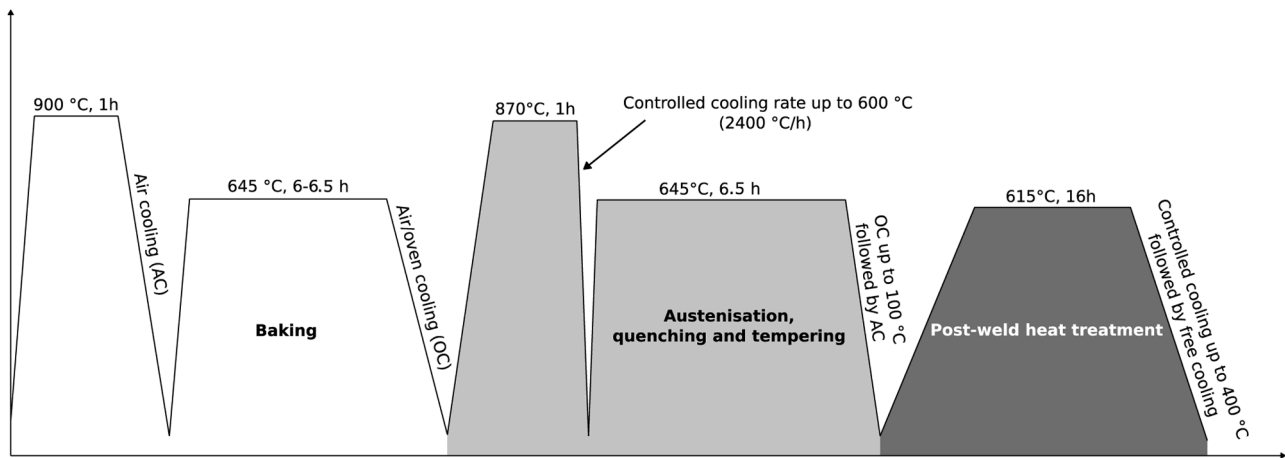


Fig. 1. Schematic representation of the heat treatments carried out after homogenization and forging.

toughness levels between 40 and 250 MPa.m^{0.5}. From Charpy and fracture toughness tests, brittle-to-ductile transition reference temperatures T_{56J} (temperature at which the CVN absorbed energy is 56 J) and T_0 (temperature at which $K_{Jc} = 100 \text{ MPa}\sqrt{\text{m}}$) were identified and used to quantify the evolution of brittle failure resistance with chemical content: a decrease in T_{56J} and/or T_0 between two states of a material indicates that the material becomes more resistant to brittle fracture.

2.3. Microstructural and fractographic analyses

To characterize the evolution of the microstructure, Electron Backscatter Diffraction (EBSD) maps of approximately 70 000 μm^2 (300 vs 225 μm , step of 0.25 μm at 20 keV) were obtained using a Jeol JSM-7001F Scanning Electron Microscope (SEM) and a Bruker eFlash detector. From these maps, the distributions of misorientation angles between two neighbouring pixels were identified for the three materials. To avoid highlighting slight misorientations, frequent inside bainitic and martensitic microstructures, angles below 2.5° were not considered in the present analyses. Based on misorientation angles, the average size of both prior austenitic grains (PAG) and ferritic grains could be estimated. As a first basic approach, a ferritic grain boundary was here defined as a misorientation angle larger than 15°, a critical value that approximately corresponds to the minimum theoretical disorientation between two ferrite grains within the same PAG [13]. According to the same reference, no disorientations between ferrite grains located inside the same PAG should be observed in the range [20;50°]. Therefore, any misorientation in this range is supposed to be the result of a grain boundary between two PAG. The traces on the EBSD map of the grain boundaries misorientations in the range [20;50°] are thus used to determine the average size of PAG.

Due to the increase in the alloying elements content (for the same quenching rate), the microstructure is expected to evolve from upper bainite towards lower bainite/martensite [3,10]. To quantify this trend, the properties of lower bainitic/martensitic microstructures reported in the literature were used to define different microstructural parameters. Authors have observed that lower bainitic/martensitic microstructures feature a higher frequency of misorientation angles between 50–60° when compared to upper/granular bainite [13,14]. It was also observed that misorientation angles associated with lower bainitic/martensitic transformation were 55° $\langle 110 \rangle$ and especially 60° $\langle 111 \rangle$ (CSL $\Sigma 3$ grain boundaries) [13]. Based on these observations, three indicators were used:

1) R, defined as the ratio of the peaks around 60 and 55° on the misorientation angle distribution;

- 2) The density of $\Sigma 3$ grain boundaries, identified using the tolerance given by the Brandon criterion [15];
- 3) μ , defined as the cumulative distribution function of misorientation angles from 62 down to 50°.

The brittle failure of low-alloyed steels is caused by the unstable propagation of a microscopic crack, which appears due to the rupture of a microscopic brittle phase [16–18]. Since this phase is often a carbide [19–23], a statistical analysis of the carbide population was carried out to identify its equivalent diameter distribution. Metallographic samples were prepared and etched using 2 % Nital for a few seconds (5–10 s) to reveal mainly the carbides. To have both a good image resolution and a representative carbide sample, 8 sequential SEM images with an amplification of 5 000x were acquired for each material. These images were combined to create a new one with approximately 31 million pixels and 3000 μm^2 of area, which was then analysed to identify the morphological properties of the carbides. To avoid artefacts, only carbides whose area was greater than 0.01 μm^2 were considered. Finally, the following adaptation of the Weibull probability density function proposed by Lee was identified in experimental results [24]:

$$\frac{dF}{dr} = \frac{2\alpha}{\beta} \left(\frac{2r - \gamma}{\beta} \right)^{\alpha-1} \exp \left[- \left(\frac{2r - \gamma}{\beta} \right)^\alpha \right], \quad (1)$$

where α , β and γ are the distribution parameters, and r is the equivalent radius of the carbide.

For the selected Charpy and CT specimens at the ductile-to-brittle transition (25–60 J and 80–175 MPa $\sqrt{\text{m}}$), fractographic analyses were performed (5 for 0.18 %C, 6 for 0.29 %C and 6 for 0.38 %C) to identify both the brittle failure mechanism (cleavage and/or intergranular fracture) and the microstructural feature at the origin of brittle failure. This microstructural feature was determined based on the crack propagation path inferred from cleavage river marks, when possible (i.e. in the absence of significant intergranular fracture). Each time a precise microstructural feature was identified, Energy-Dispersive X-ray spectroscopy (EDX) was carried out for a qualitative analysis of its chemical composition using a Bruker XFlash 6–30 detector. To minimize the influence of matrix composition on the EDX spectra of such small microstructural features (typically a few tenths of a micron), a sensitivity analysis was carried out, from which the following parameters were obtained: acceleration voltage of 10 keV, dead time of 20–40 % and 1–2 million counts per spectrum.

3. Experimental results

3.1. Mechanical tests

The true stress-plastic strain curves of the three materials are presented in Fig. 2a–c, whilst the evolution of yield stress with the temperature is presented in Fig. 2d. The yield stress evolution is described with a two terms equation: one does not depend on the temperature and the other one does. For the same carbon content, the yield stress increases when the temperature is reduced. This trend is especially important at 0.38 %C, tested at smaller temperatures, whilst a weaker dependence on the temperature is observed at 0.29 %C. At a given temperature, yield stress also increases as the carbon content rises. This evolution can potentially be explained by the evolution of both the carbide population and the ferritic grain size, which will be further discussed in a subsequent subsection. One should notice the presence of Lüders bands for all materials, which persist after the initial yield until ϵ^p increases from about 1 to 2 % with the decrease of the test temperature.

The results of both Charpy and fracture toughness tests are presented in Fig. 3a and b. As expected, the upper shelf energy of Charpy curves decreases with the carbon content, which is likely related to the increase in the carbide density that promotes the growth and coalescence of cavities initiated on relatively large non-metallic inclusions. In the transition regime, an unexpected evolution of T_{56J} and T_0 (Fig. 3c) is

observed: the highest resistance against brittle failure (i.e. lowest reference temperatures) is observed for 0.38 %C, whilst similar resistances are observed at 0.18 and 0.29 %C. This result is somehow surprising since macrosegregation in large forgings has usually been associated with the embrittlement of ferritic steels such as pressure vessel steels [1,3,5]. The possible explanations for this unusual behaviour will be discussed in detail in Section 5.

3.2. Fractographic analyses

A summary of the fractographic analysis results is shown in the Appendices (Tables A1 and A2). These analyses indicate that the brittle fracture mechanism depends on the carbon content, as shown in Fig. 4. For the materials with 0.18 and 0.29 %C, transgranular cleavage is the dominant mechanism, whilst a mix of transgranular cleavage and intergranular fracture is observed for the material with 0.38 %C (Fig. 4). Due to the significant presence of intergranular failure at 0.38 %C, initiation sites could not be identified on this alloy. For the other two materials, the microstructural feature at the origin of cleavage fracture is predominantly carbides (8/11). Most of these are enriched with Molybdenum and Manganese (6/8), as indicated in Fig. 5. The equivalent diameter of the carbides at the origin of brittle failure ranged from 0.20 to 0.80 μm . This result is consistent with recent literature results in which large and brittle carbides at grain boundaries were identified as

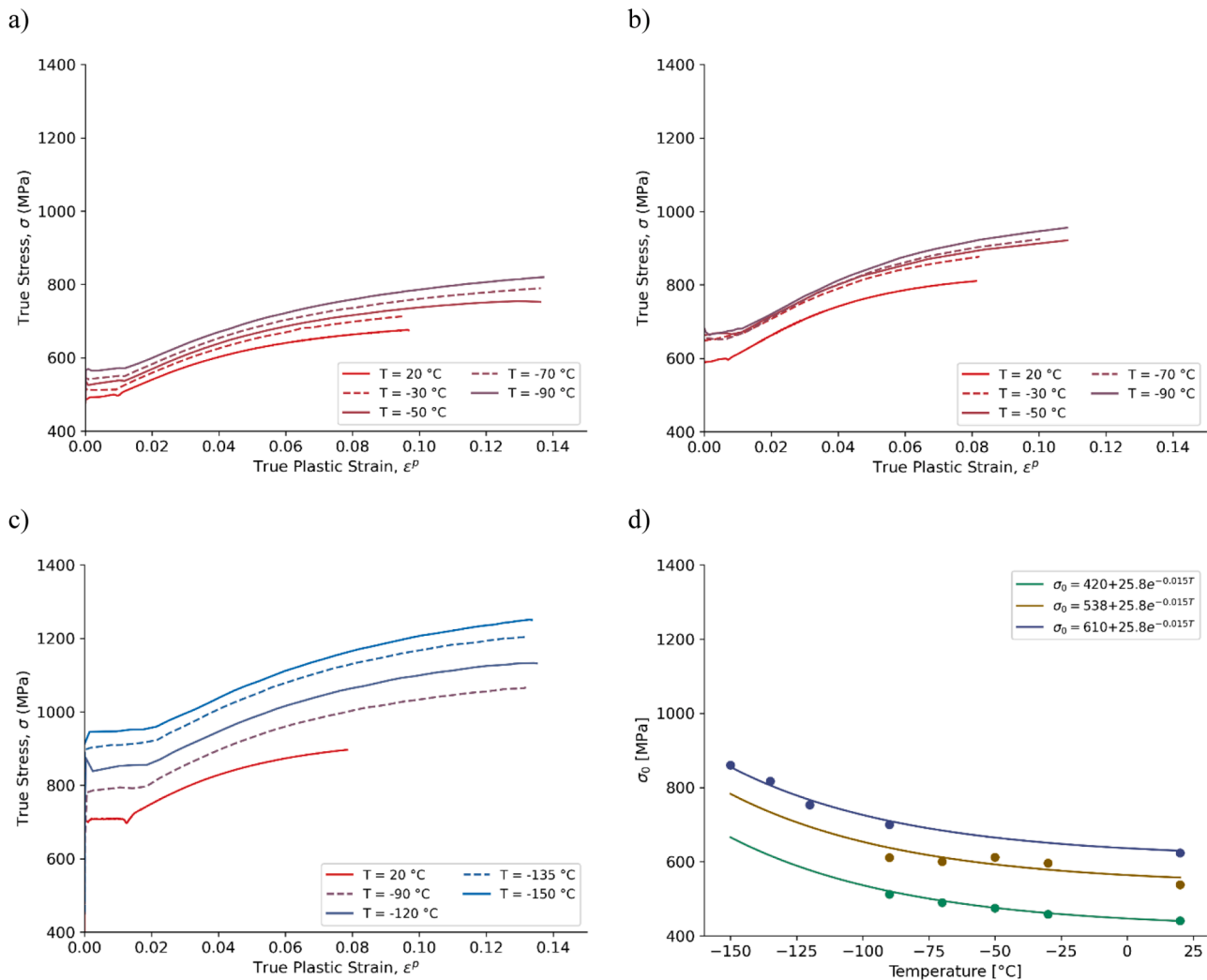


Fig. 2. True stress vs true plastic strain curves before necking at (a) 0.18 %C, (b) 0.29 %C and (c) 0.38 %C and (d) evolution of the yield stress with the temperature for all three materials.

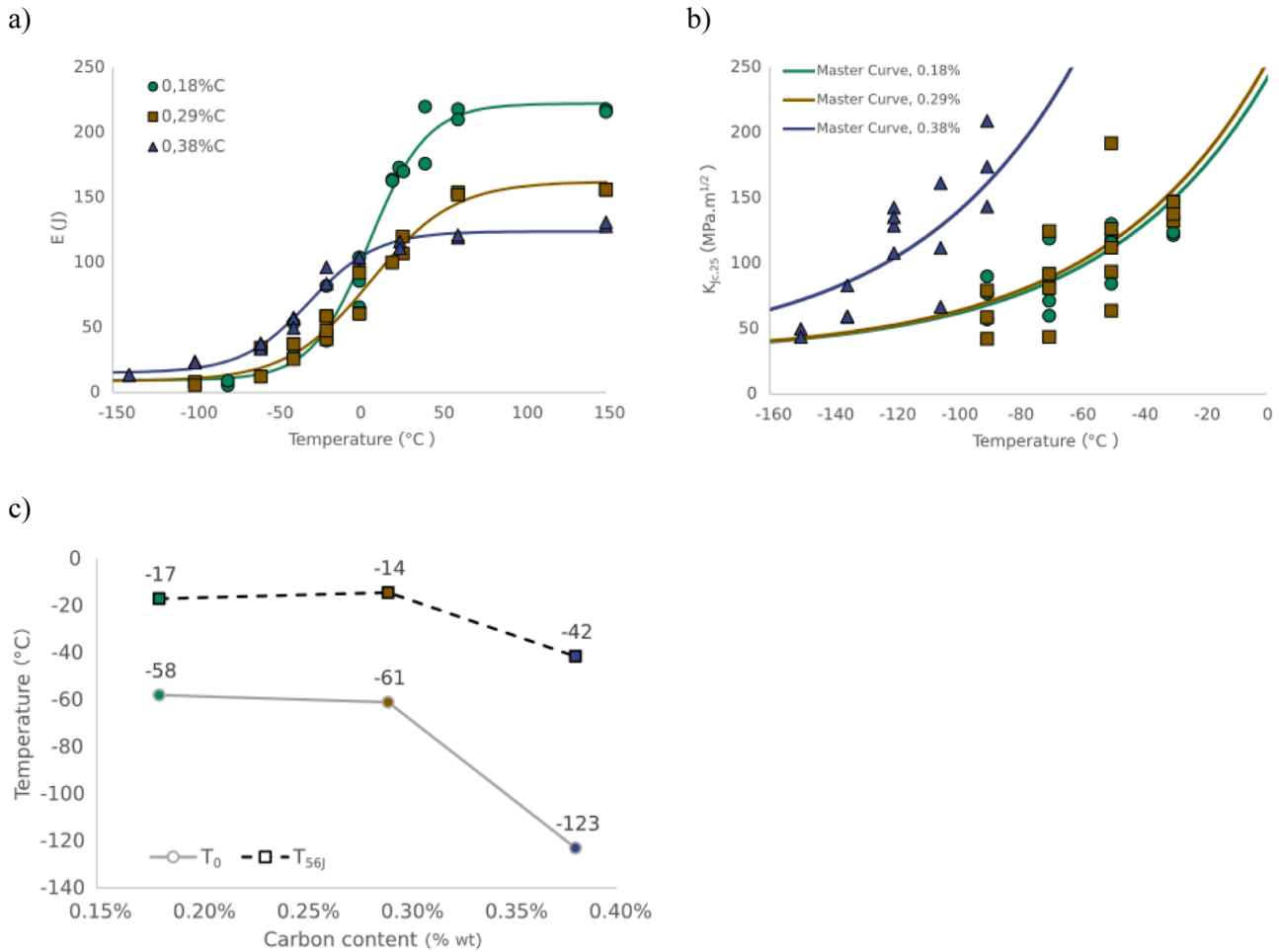


Fig. 3. Evolution of the (a) absorbed energy from Charpy tests, (b) fracture toughness and (c) T_{56J} and T_0 with the carbon content.

the microstructural elements at the origin of brittle failure of low-alloyed steels [19,20,23]. Note that all those carbides triggering macroscopic brittle fracture are found in the current study near the interface of two or more cleavage facets, suggesting that carbide localisation also plays a role in the initiation of brittle failure. For the remaining cases (4/11), featureless initiation sites—classified as possible grain boundaries and rough facets—are identified (Fig. 6).

3.3. Microstructural characterization

The EBSD images obtained for the three materials are presented in Fig. 7a–c, and the associated misorientation angles distributions are presented in Fig. 7d. Qualitatively, the results presented in Fig. 7a–c indicate that the microstructure evolves as expected towards a lath-like microstructure, likely lower bainitic/martensitic, when the carbon content is increased. This is quantitatively confirmed by the evolution of the microstructural parameter μ , the percentage of $\Sigma 3$ grain boundaries and the R parameter (Fig. 8).

The average size of prior austenitic grains deduced from EBSD maps is similar for the three materials, ranging from 31–37 μm . These values are consistent with those reported in the literature [7,11] for this class of materials. However, the average size of ferritic grains decreases as the carbon content increases, as presented in Fig. 9. This reduction, associated to a better hardenability, may partially explain the increase in the yield stress with carbon content presented in Fig. 2d due to a possible Hall-Petch effect, in addition to hardening by thin carbides like M_2C [25, 26]. Note, however, that a comparison with the ferritic grain sizes observed in the previous investigation [8,9] (which were almost

independent of carbon content) suggests that the current result is not a simple effect of a variation in the chemical composition itself but is probably also associated with differences between the thermomechanical processing routes applied in these two studies. The increase in the ferritic grain size of the present investigation may lead to an embrittlement, as indicated by previous results reported in the literature [27–29]. The comparison between ferritic grain sizes presented in Fig. 9 suggests that this effect should be especially pronounced at 0.18 %C.

The evolution of the equivalent diameter distribution of carbides with carbon content is shown in Fig. 10a, and the parameters of the Lee-Weibull distribution are shown in Table 2. It is also observed that the carbide surface fraction—all carbide sizes comprised—increases with carbon content, as expected. Consequently, a part of the yield stress increase due to the Orowan mechanism is expected to increase with the carbon content, which is consistent with the results presented in Fig. 2d. However, one can see that large carbides are less predominant for materials with the highest carbon contents than for the 0.18 %C material. Since fractographic analyses indicate that only carbides greater than 0.2 μm seem to play a role in brittle failure initiation, an *ad hoc* distinction between large ($\geq 0.2 \mu\text{m}$) and small ($< 0.2 \mu\text{m}$) carbides is proposed. To consider the combined effects of the evolution of distribution and carbide surface fraction with carbon content, the number of both total and large carbides for the same surface area is presented in Fig. 10b. It is observed that large carbides population is greater at 0.18 %C, despite the smaller total carbide population. Due to the change in the carbide size densities with carbon content, most of the carbides of the materials with the highest carbon content are too small to induce brittle failure. Hence, the carbon content increase is expected to reduce the number of

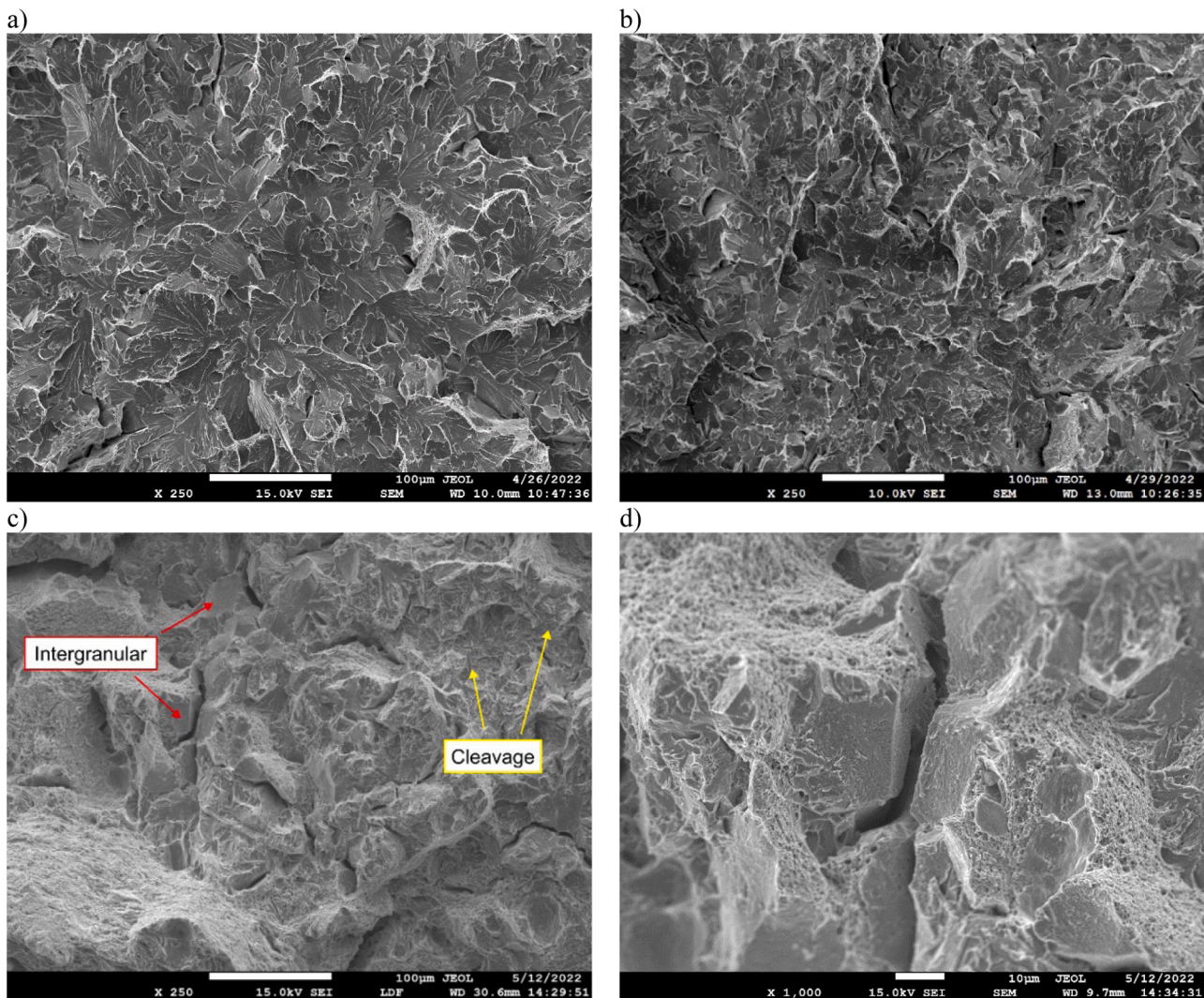


Fig. 4. Typical brittle fracture mechanisms observed for the three materials: (a) cleavage at 0.18 %C (39,9 J at -20 °C), (b) cleavage at 0.29 %C (25,7 J at -40 °C) and (c) mix of cleavage and intergranular fracture at 0.38 %C (57,0 J at -40 °C). (d) A detailed view of intergranular fracture presented in (c).

potential initiation sites in this case [27,30–32], leading, from the brittle fracture point of view, to a strengthening effect rather than the embrittlement usually expected by the increase of the carbides total number density.

As previously discussed, Mo and Mn-enriched carbides were the predominant microstructural element at the origin of brittle failure. Similar type of carbides has been characterized on other model alloys as cementite containing different %wt of Mn and Mo [33]. More recently, on industrial materials, carbides with similar Mn and Mo contents have been characterized as M_3C but also as $M_{23}C_6$ carbides [23]. In a first attempt to describe qualitatively the proportion of Mo-enriched carbides, the EDX spectra of 20 carbides chosen randomly at multiple intergranular facets of the fractographic surface as the one shown in Fig. 6b are obtained. The number of carbides analysed was 5, 7 and 8 for the materials at 0.18, 0.29 and 0.38 %C, respectively. The resulting EDX spectra are presented in Fig. 11, in which only the spectra envelopes are presented for the sake of visual clarity. Little variation is observed between the Mo peaks for the three materials, suggesting the Molybdenum content of these carbides does not vary significantly between materials. Due to this similarity, the three envelopes can thus be combined and compared to the EDX spectra of carbides found at initiation sites at 0.18 and 0.29 %C. As shown in Fig. 12, these random carbides do not feature the pronounced Molybdenum peaks observed for the majority (5/6) of the carbides found at initiation sites. In addition to their particular

chemical composition, the smallest carbides identified at an initiation site were larger than 84.6 % and 99.8 % of all carbides used for the morphological analyses at 0.18 and 0.29 %C, respectively. Finally, all of them were found at the interface of the cleavage facets, which are likely prior austenitic grain boundaries [23,30]. All these observations suggest that brittle failure initiation is controlled in these materials, apart from small inclusions, by the relatively rare large Mo-enriched carbides located at grain boundaries that could be prior austenitic grain boundaries, and that other carbides do not play an important role in it.

4. Modelling

4.1. Critical fracture stress

As discussed in the previous section, the lowest transition temperatures are observed at 0.38 %C, for which a lower bainitic/martensitic microstructure is observed. For this class of RPV steels, martensitic microstructures may indeed sometimes exhibit lower transition temperatures than upper bainitic ones after tempering [34]. In the present study, both the ferritic grain size reduction and the decrease in the large carbide population suggest that a higher carbon content may lead to a microstructure that is globally more resistant to cleavage failure for these homogenized model materials. To verify this hypothesis, a critical fracture stress is calculated from instrumented impact Charpy tests using

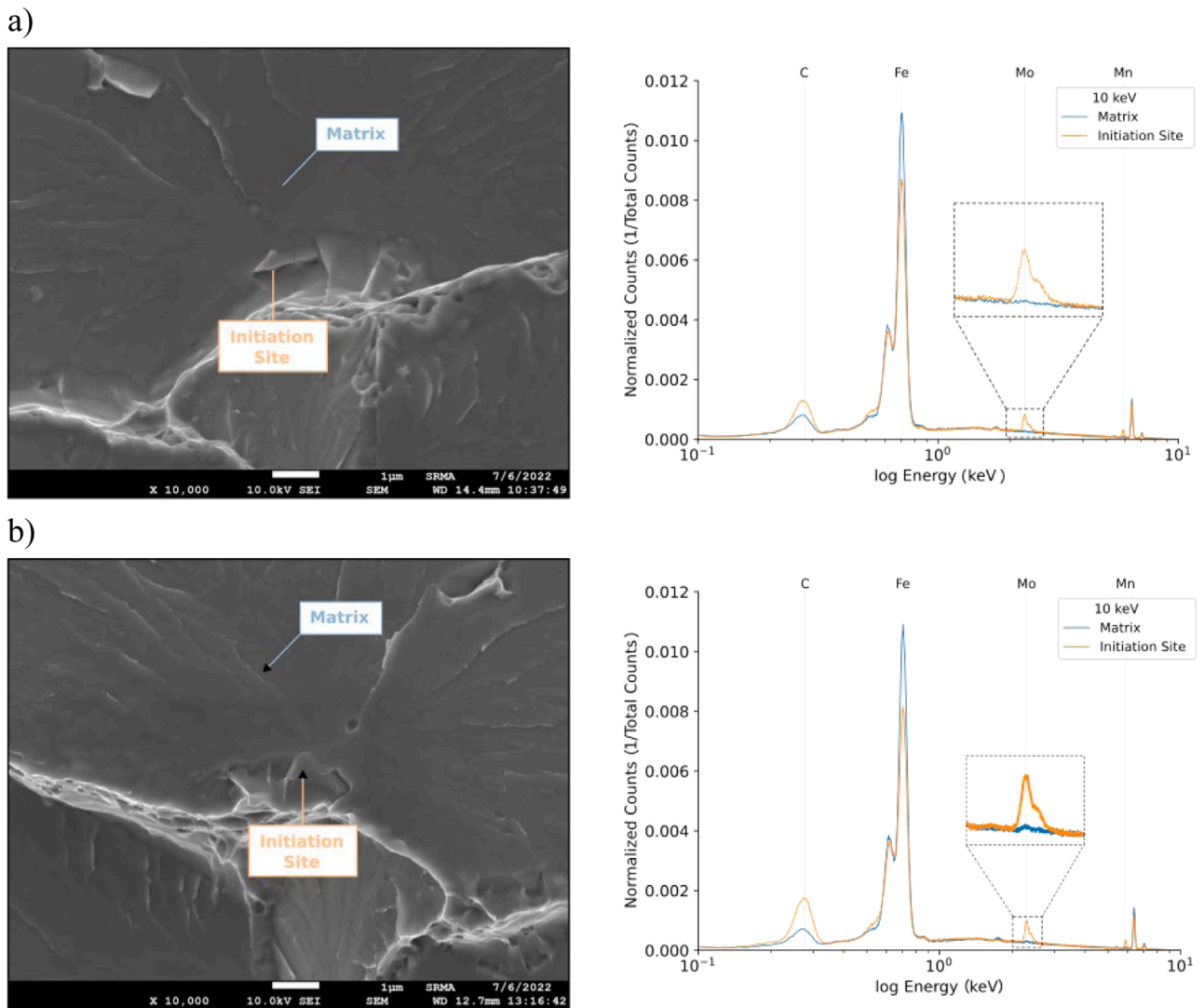


Fig. 5. Initiation site identified as a Molybdenum/Manganese-enriched carbide (CT specimen with 0.29 %C, 146 MPa√m at -30 °C, both half-specimens).

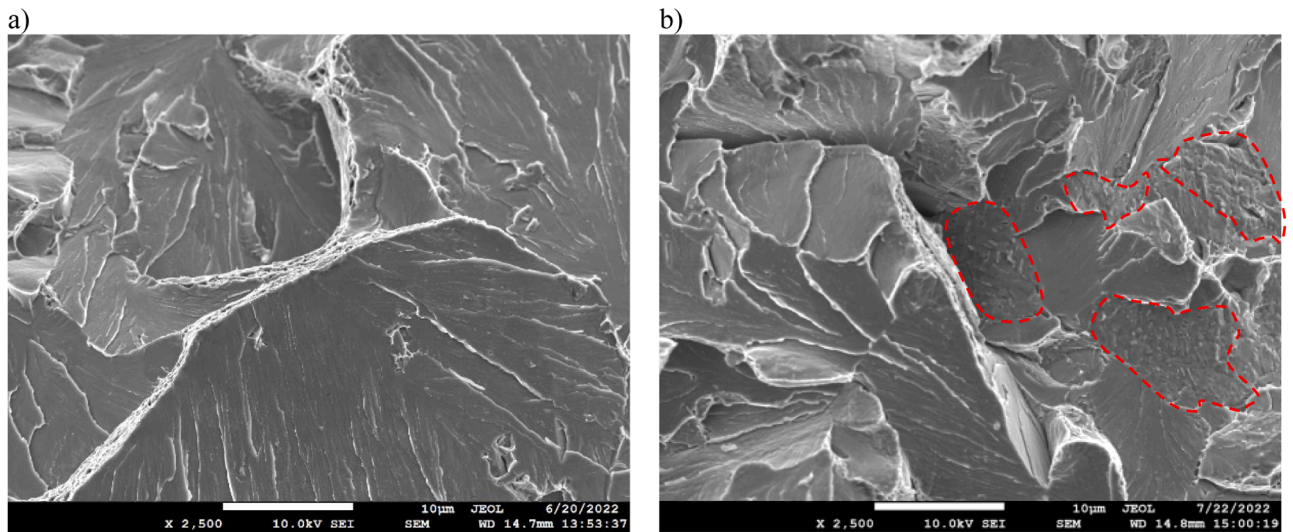


Fig. 6. “Featureless” initiation sites: (a) possible grain boundary (CT specimen with 0.18 %C, 116,2 MPa√m at -50 °C) and (b) rough facets circled in dash-red lines (CT specimen with 0.29 %C, 80 MPa√m at -90 °C.).

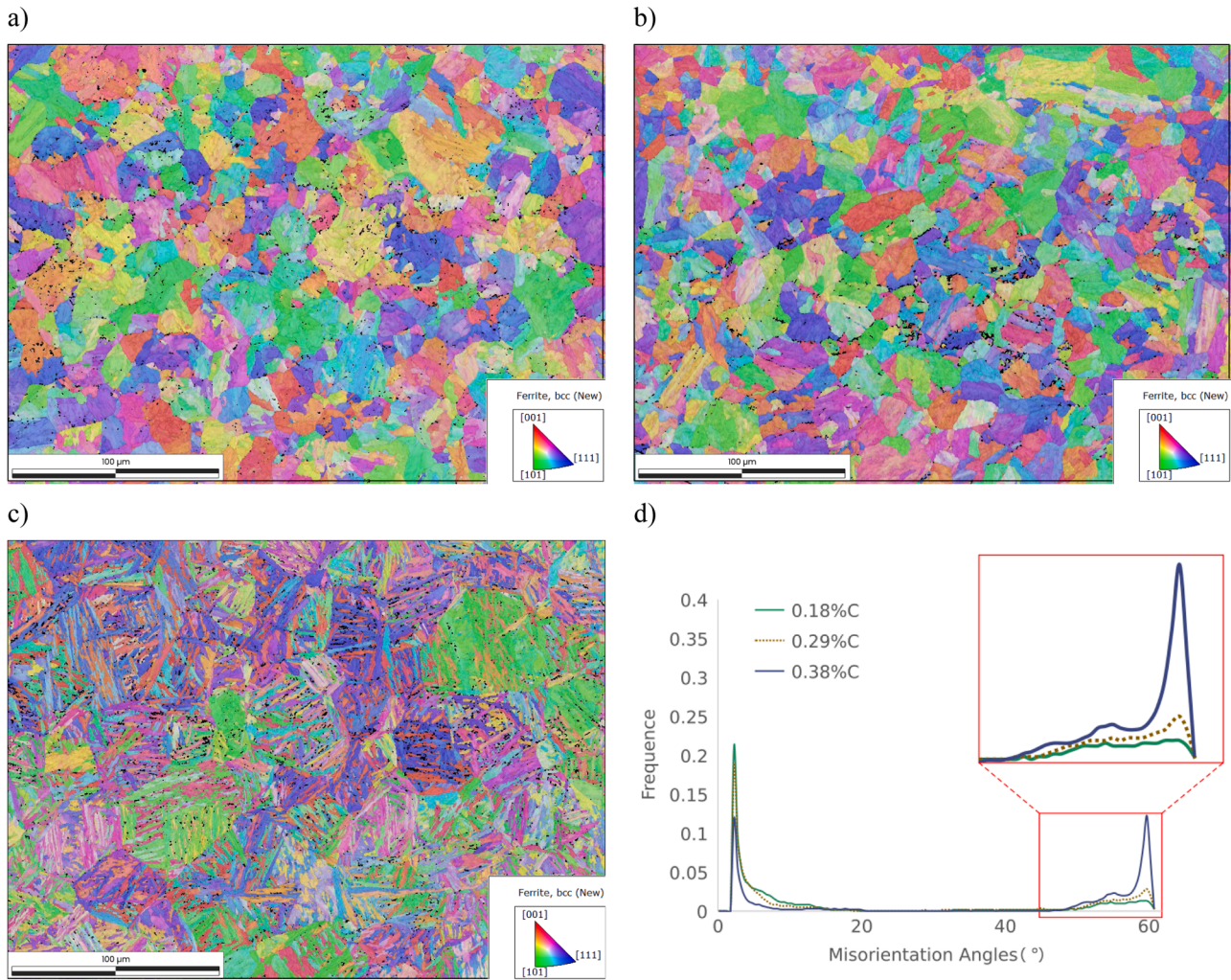


Fig. 7. Evolution of the microstructure with the chemical composition: (a) 0.18 %C, (b) 0.29 %C, (c) 0.38 %C and (d) evolution of misorientation angles obtained from EBSD analyses.

the methodology proposed by [35].

The critical fracture stress is the theoretical stress level at which failure occurs at the onset of plastic deformation of the sample. In this case, a limited amount of plastic deformation is present, only enough to induce the rupture of the brittle microscopic phase at the origin of failure. Since failure is (almost) exclusively brittle, the value of the critical fracture stress is an indirect measure of the brittle fracture resistance of a given microstructure: an increase in the critical stress indicates that the microstructure becomes more resistant to purely brittle failure. The critical fracture stress can be estimated from Charpy instrumented tests as illustrated in Fig. 13. First, the values of the maximum force (P_m) and the force at general yield (P_{gy}) of each test are recorded (Fig. 13a). Afterwards, the evolution of both P_m and P_{gy} with the temperature is determined (Fig. 13b). When $P_m = P_{gy}$, failure occurs at the onset of plastic deformation, and the critical fracture stress can thus be estimated using the following expression [35]:

$$\sigma^* = (2.35)(45.8)P^* \quad (1a)$$

in which P^* is the force for which $P_m = P_{gy}$ at the temperature T^* .

The evolution of P_m and P_{gy} with temperature for the three materials is presented in Fig. 14a-c. For a few tests, failure occurred before a significant deviation from the linear stage of the force vs. time curve (grey zone in Fig. 13a). For these cases, P_{gy} could not be determined and only P_m is presented. The value of P^* used to estimate the critical stress is thus the intersection point of both fit curves, as schematically illustrated

in Fig. 13b. Note that the intersection points obtained by this methodology are nonetheless consistent with the values of P_m that could be directly extracted from raw data in the cases where such data are available in this intersection region (0.18 %C and especially 0.38 %C). From these values of P^* , the evolution of the critical fracture stress with the carbon content is computed and shown in Fig. 14d. The critical stress increases with the carbon content, suggesting that the microstructure becomes indeed more resistant to brittle failure with the increase in carbon content for these homogenized microstructures. It is worth noting that the curvature of the P_m curve changes as the carbide content increases, and even changes from concave to convex in the case of the highest carbon content.

4.2. Beremin model

For the probabilistic description of fracture toughness K_{Jc} , the Beremin model is used [16]. In the present paper, only a brief description of this model is presented. For the Beremin model, the failure probability of the specimen can be calculated as

$$P_r = 1 - \exp \left[- \left(\frac{\sigma_w}{\sigma_u} \right)^m \right], \quad (2)$$

in which m and σ_u are material constants to be determined, and σ_w is the Weibull stress, calculated as

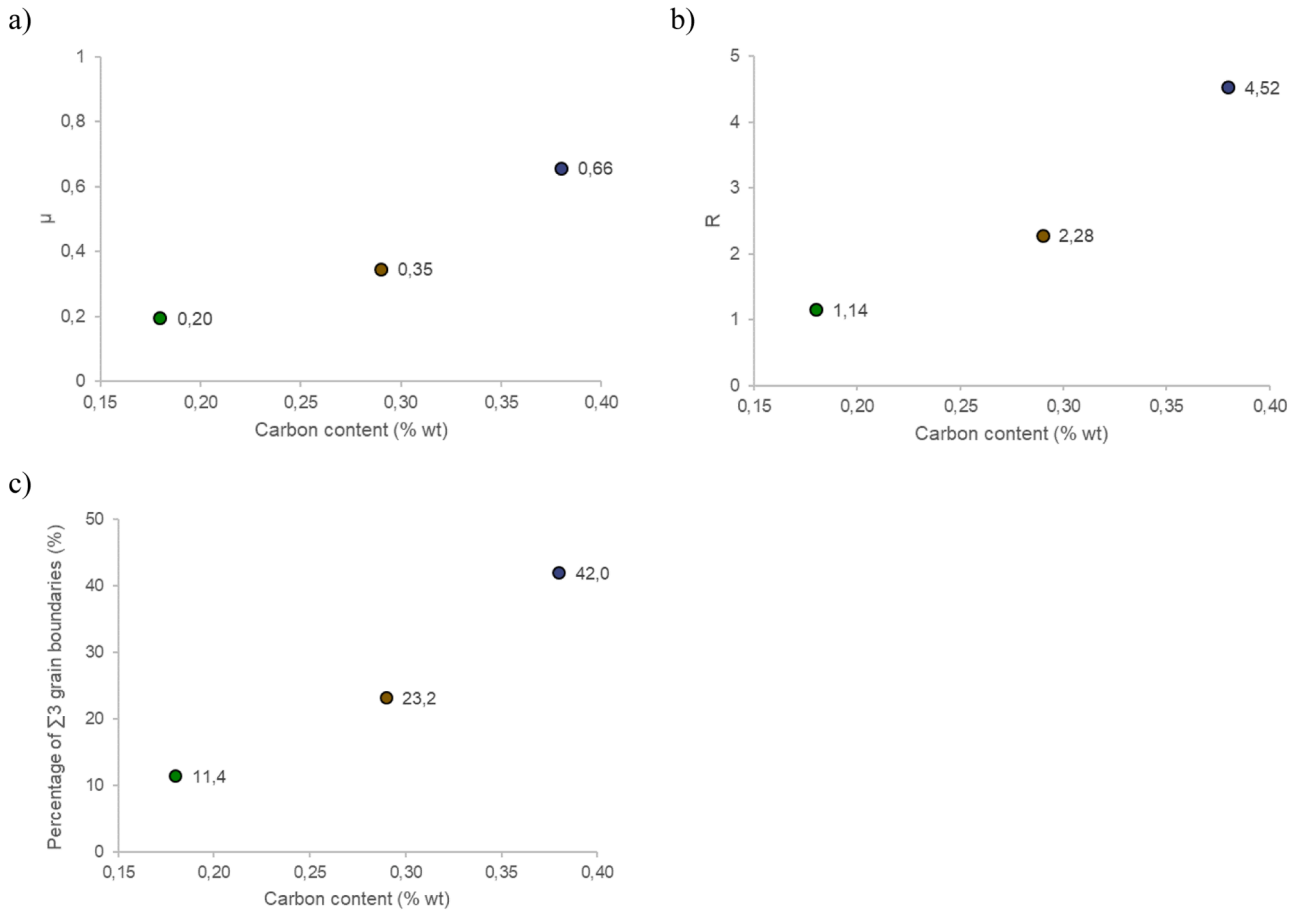


Fig. 8. Evolution of (a) microstructural parameter μ , (b) parameter R and (c) the percentage of $\Sigma 3$ grain boundaries with carbon content.

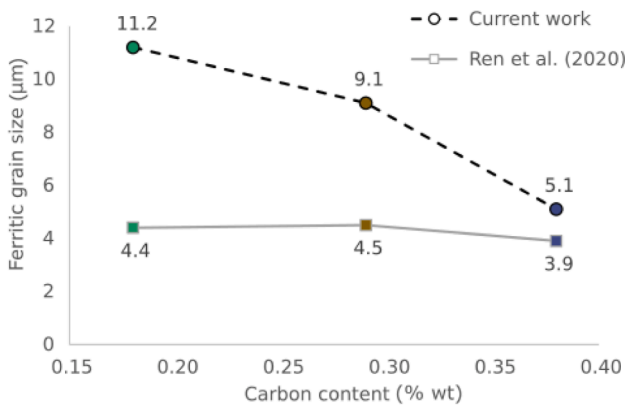


Fig. 9. Evolution of the average ferritic grain size with carbon content.

$$\sigma_w = \sqrt[m]{\sum_i^k (\sigma_i^1)^m \frac{V_i}{V_0}} \quad (3)$$

where k is the number of elements in which the plasticity has been activated (i.e. $p > 0$), σ_i^1 is the maximal principal stress applied on the element of volume V_i , and V_0 is the representative volume in which the continuum mechanics approximation is valid, here assumed to be $125\,000\ \mu\text{m}^3$ ($50 \times 50 \times 50\ \mu\text{m}$), which corresponds approximately to 8 prior austenitic grains (Fig. 9).

To compute the Weibull stress σ_w and the corresponding value of K_{Jc} , Finite Element Analyses have been carried out using CAST3M software

(edition 2021), with a mesh identical to the one used by [8]. To better capture the stress gradients at the vicinity of the crack tip, a finer mesh consisting of 20 node brick elements (CU20 in CAST3M) of $50 \times 50 \times 50\ \mu\text{m}$ was used at this region. Note that this element size is consistent with the representative volume V_0 adopted for the Beremin model. The value of K_{Jc} is computed for each loading step based on the J-integral values obtained using numerical integration (GTHETA method in CAST3M). The plastic behaviour of the material is modelled by the same set of constitutive equations as in [8,9]:

$$\sigma(\varepsilon^p) = \sigma_{y0} + Q_1[1 - \exp(-b_1\varepsilon^p)] + Q_2[1 - \exp(-b_2\varepsilon^p)], \quad (4)$$

in which

$$\sigma_{y0}(T) = \sigma_a + \sigma_T \exp\left(-\frac{T}{T_y}\right), \quad (5)$$

$$Q_1 = -p_1 T + p_2, \quad (6)$$

$$b_1(T) = 26 + 0.095T. \quad (7)$$

The first term of Eq. (4) describes the evolution of the yield stress with temperature; the second, the hardening behaviour at small deformations, assumed to be temperature-dependent; and the third, the hardening behaviour at large deformations, assumed to be temperature-independent. Material parameters (Table 3) have been identified from tensile tests at multiple temperatures without considering the Lüders bands. The difference between experimental and simulated tensile curves obtained using the calibrated parameters presented in Table 3 is less than 5 % (in terms of stress level for a given plastic strain). Since tensile tests can only be used before necking of the specimen, constants Q_2 and b_2 could not be directly determined and are assumed to be

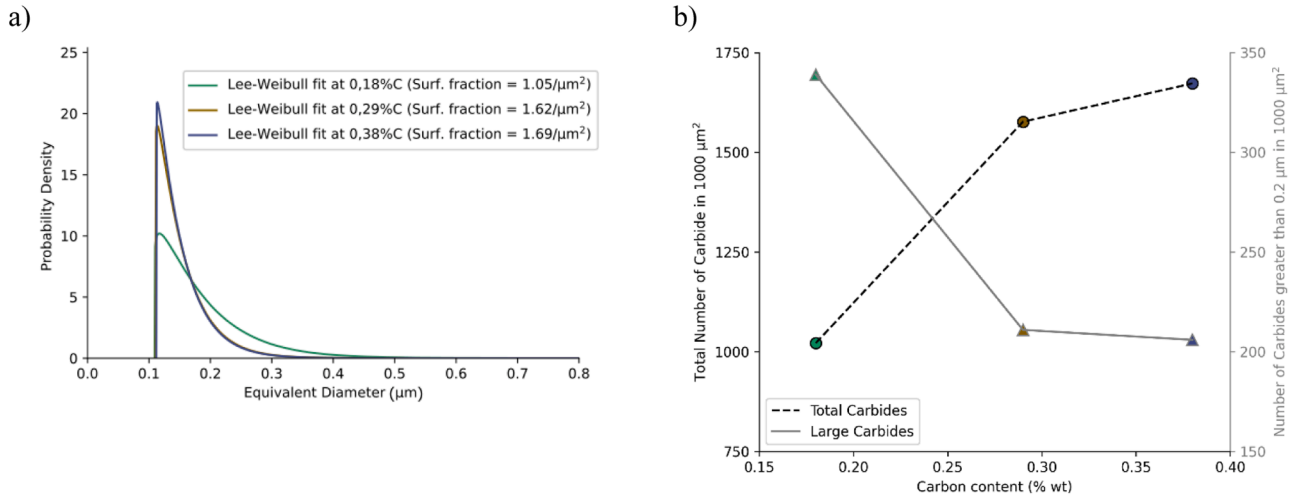


Fig. 10. Evolution of (a) equivalent diameter distribution and (b) number of total and large (> 0.2 μm) carbides with carbon content.

Table 2

Parameters of the Lee-Weibull distribution and of carbide analyses.

Material	α	β (μm)	γ (μm)	Surface fraction (μm^{-2})	Total carbides
0.18 %C	1.084	0.081	0.109	1.05	3305
0.29 %C	1.055	0.045	0.111	1.62	4666
0.38 %C	1.034	0.043	0.112	1.69	5436

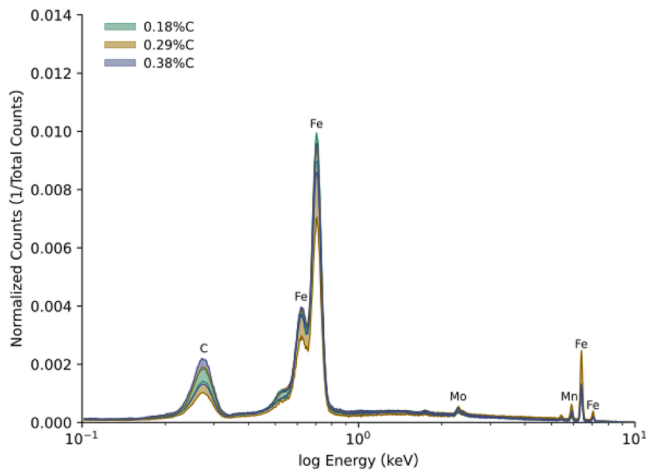


Fig. 11. EDX envelopes obtained from random carbides (5 carbides for 0.18 % C, 7 for 0.29 %C and 8 for 0.38 %C).

identical to those identified by [8,9]. A comparison between experimental and simulated force vs CMOD curves is presented in Fig. 15, in which only one representative experimental curve is plotted for the sake of visual clarity. The results indicate that FE simulations tend to slightly overestimate the force response, especially for the 0.38 % at -90 °C. Nonetheless, the relative error (at a specific CMOD) is inferior to 8 % for all cases.

The parameters m and σ_u are determined as follows. Due to the low number of experimental fracture toughness results, a usual value of $m = 20$ is adopted for all materials, which is consistent with the values reported in the literature for RPV steels [16,36,37]. The value of σ_u is determined based on the evolution of the median K_{Jc} —which corresponds to the experimental fracture probability P_r of 50 %—with test temperatures. Multiple values of σ_u are pre-selected and, together with the values of σ_w obtained from FEA, are used to calculate the K_{Jc}

corresponding to the simulated $P_r = 50$ %. The retained value of σ_u is the one that produces the best fit of the median K_{Jc} evolution. The isoprobability curves for the three materials are presented in Fig. 16a–c. The results of the simulations show that the value of σ_u linearly increases with the carbon content, as shown in Fig. 16d.

In an attempt to better understand the physical meaning of this trend, the analytical expression derived from the Beremin model that relates the failure probability P_r to the yield stress σ_{y0} , the fracture toughness K_{Jc} , and the parameters m and σ_u can be used [16]:

$$\ln\left(\frac{1}{1 - P_r}\right) = \frac{\sigma_{y0}^{m-4} K_{Jc}^4 B C_m}{V_0 \sigma_u^m}, \quad (8)$$

in which B is the specimen thickness (i.e. crack front length), C_m is calculated from the HRR stress field [38,39] and V_0 is the representative volume. When $T = T_0$, $P_r = 0.5$, $K_{Jc} = 100 \text{ MPa}\sqrt{\text{m}}$ and for $B = 25 \text{ mm}$, the relation between σ_u and σ_{y0} can be written as

$$\sigma_u = C \sigma_{y0}^{(m-4)/m} = C \left[\sigma_a + \sigma_T \exp\left(\frac{T_0}{T_y}\right) \right]^{(m-4)/m}, \quad (9)$$

where C is a constant depending only on C_m and V_0 . This equation can finally be rewritten as

$$T_0 = -T_y \ln\left(\frac{1}{\sigma_T} \left[\left(\frac{\sigma_u}{C}\right)^{m/(m-4)} - \sigma_a \right]\right) = -T_y \ln\left[\frac{1}{\sigma_T} (\sigma_u - \sigma_a)\right]. \quad (10)$$

Eq. (10) indicates that T_0 evolution with the carbon content is the result of a competition between two phenomena: the evolution of the microstructural resistance against brittle fracture (represented by σ_u , which includes parameters m and σ_u) and the evolution of the yield stress (represented by parameters σ_a , σ_T and T_y). If we make the thought experiment that there is no significant evolution of the microstructural resistance with the carbon content (i.e. σ_u is constant), T_0 evolution should be governed mainly by the yield stress evolution. Assuming reasonably that σ_T and T_y remain almost constant and that σ_a bears the carbon content effect (Table 3), an increase of T_0 with carbon content should be observed. This scenario is compatible with reports in the literature that macrosegregation can lead to an embrittlement of RPV steels [1–6]. In the present investigation, however, the carbon content increase is associated with a significant microstructural evolution (i.e. reduction of large carbide population, reduction of the ferritic grain size and evolution towards lower bainite/martensite crystallographic microstructure) that is beneficial in terms of resistance to brittle fracture. Such a microstructural evolution results in an increase of σ_u (i.e. σ_u for a constant value of m) with carbon content, explaining the observed

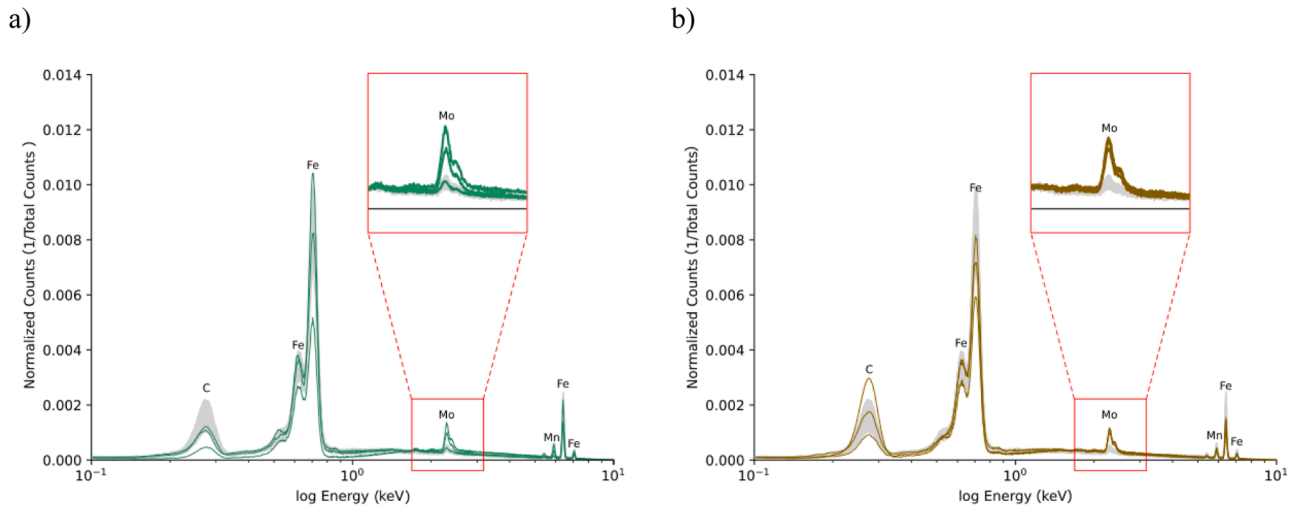


Fig. 12. Comparison between the EDX spectra of random carbides (in grey) and of carbides at initiation sites (in colour) at (a) 0.18 %C, (b) 0.29 %C.

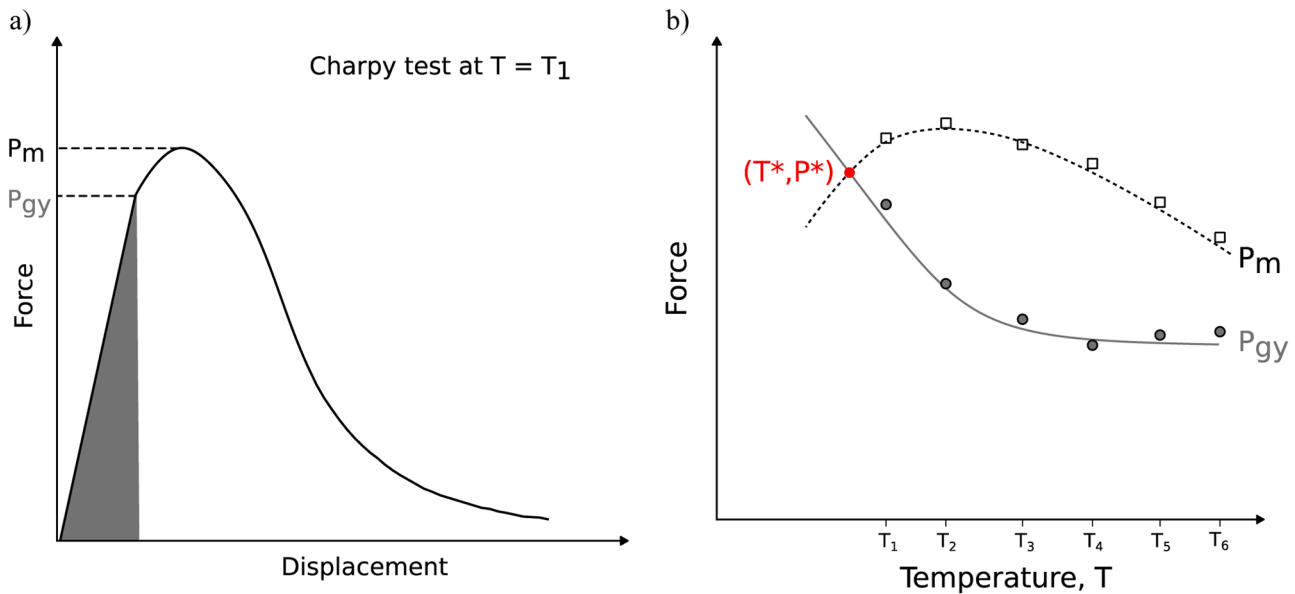


Fig. 13. (a) Definition of P_{gy} and P_m based on a schematic representation of an instrumented Charpy test and (b) evolution of P_{gy} and P_m with temperature.

decrease of T_0 . This interpretation is thus consistent with the critical fracture stress evolution presented in Fig. 13d, which is similar to the one observed for σ_u for a constant value m (Fig. 16d). Finally, it is worth mentioning that the σ_u values obtained using Eq. (10) (with experimental T_0 values, parameters of Table 3 for material yield stress, a Beremin m parameter equal to 20, and a C_m parameter of Eq. (8) equal to the one given in Beremin original paper [16]) are very similar to those obtained from complete analyses of FE simulations, with a relative difference of less than 2%. This result reinforces the validity of Eq. (10) to be used, at least, as a first guess in an identification process of parameters m and σ_u in cases where T_0 has already been determined experimentally.

5. Further discussions

As previously discussed for 0.18 and 0.29 %C materials, brittle failure initiation is mainly controlled by the relatively rare large Mo and Mn-enriched carbides located at the interface of cleavage facets. To explain this phenomenon, three (non-mutually exclusive) hypotheses are proposed. The first one is that carbides at the interface of cleavage

facets, which could be former austenitic grain boundaries [23,30], are larger than intragranular ones. Thus, the large microcracks originating from the brittle fracture of these carbides are those that lead to unstable propagation. The second hypothesis is that the presence of Mo changes the mechanical properties of these carbides. As reported by [40,41], the increase in Mo content leads to an increase in the hardness of the cementite. Consequently, the Mo-enriched carbides observed at the initiation sites may be more brittle than the standard Fe_3C . This hypothesis is in line with a previous experimental investigation that associated upper-nose temper embrittlement of A533 gr. B steel with the precipitation of large Mo-enriched $M_{23}C_6$ carbides [21], whose mechanical properties also depend on the Mo content [42]. The third one is that local stress fields at grain boundaries are more severe, which favours the rupture of intergranular carbides over intragranular ones. The first two hypotheses can be assessed based on additional morphological, crystallographic and chemical analyses of those carbides, whilst the third one could be assessed by full-field crystal plasticity simulations [43].

The intergranular fracture was present mainly at 0.38 %C, the material that exhibits the lowest transition temperatures (i.e. the highest

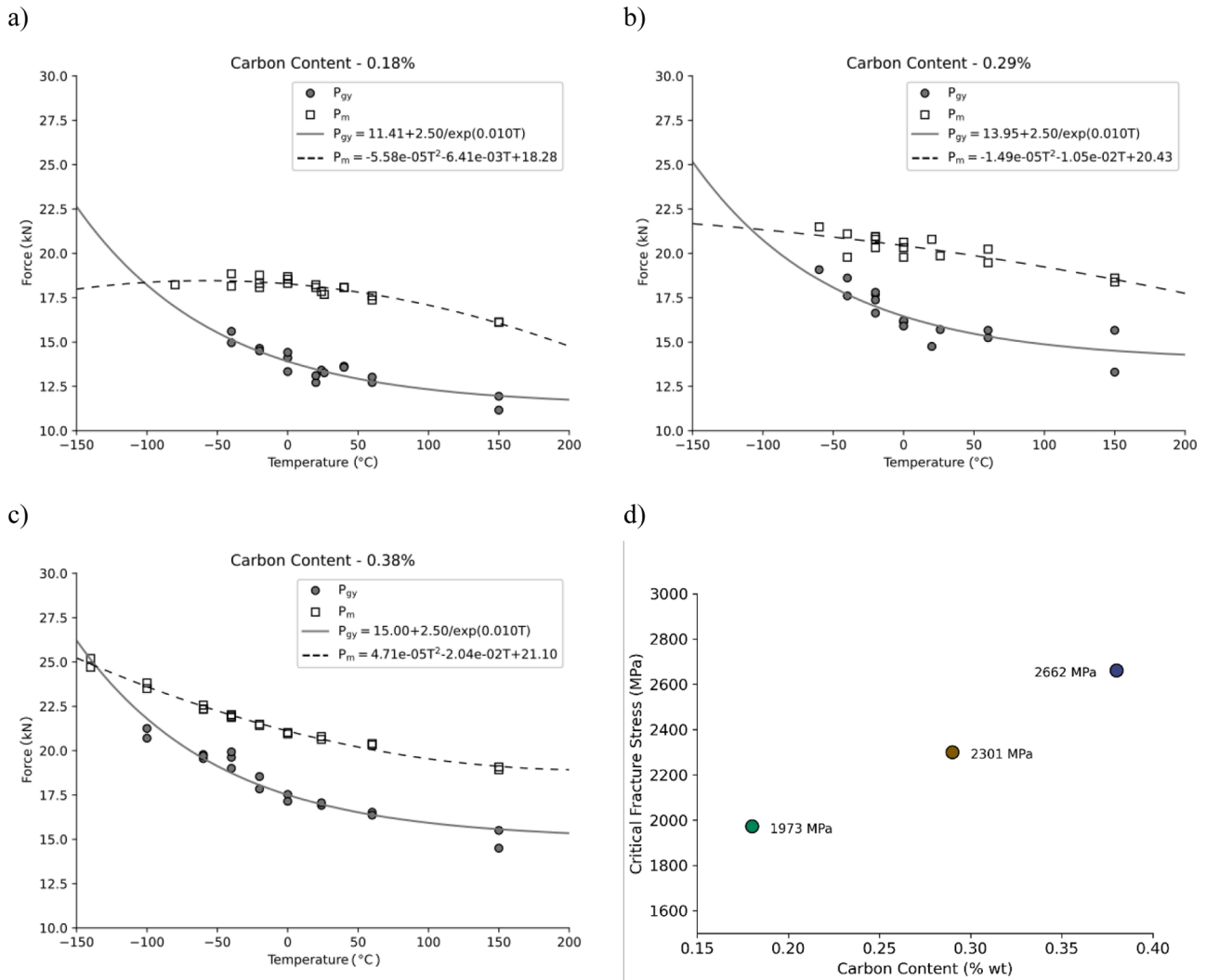


Fig. 14. Evolution of the maximum force (P_m) and the force at general yield (P_{gy}) with temperature at (a) 0.18 %C, (b) 0.29 %C and (c) 0.38 %C, and (d) evolution of the critical stress with the chemical composition.

Table 3
Material constants used for FEA.

Material	E (GPa)	ν	σ_a (MPa)	σ_T (MPa)	T_y (°C)	p_1 (MPa/°C)	p_2 (MPa)	Q_2 (MPa)	b_2
0.18 %C	205	0.3	420	25.8	66.67	0.62	230	900	0.37
0.29 %C	205	0.3	538	25.8	66.67	1.16	270	900	0.37
0.38 %C	205	0.3	577	23.2	58.82	1.42	231	900	0.37

fracture toughness at a given temperature). This result can be counter-intuitive since intergranular fracture is often associated with grain boundary embrittlement and, therefore, with an increase of transition temperatures T_0 and T_{56J} [44–47]. We believe that the microstructural evolution may explain the presence of intergranular fracture without embrittlement for this material as follows. First, the number of potential initiation sites decreases due to the reduction of the large carbide population. Second, the cleavage resistance is significantly improved due to both ferritic grain size reduction and evolution towards lower bainite/martensite. Therefore, intergranular fracture can be observed because of the substantial increase in the cleavage fracture resistance, which eventually tends to be higher than the intergranular one. This interpretation suggests that extensive grain boundary embrittlement is not at the origin of the intergranular fracture observed in the present case since embrittling elements like phosphorus are at very low level.

It is proposed that the unusual evolution of brittle fracture toughness with the chemical enrichment level observed on the homogenized materials in this work can be explained by a combination of mechanical and microstructural effects, as illustrated in Fig. 17:

- 1) From a mechanical perspective, yield stress increases with the carbon content. This is due to the combination of three microstructural effects: the increase in the carbide fraction, which likely leads to an increase in the M_2C hardening carbide fraction, the decrease of ferritic grain size and, to some extent, the increase of disorientation between the crystallographic units. When the yield stress increases, the plastic zone around the crack tip is reduced as well as the fracture process zone, but the stress level inside the process zone increases. Hence, carbides inside the process zone are submitted to higher local

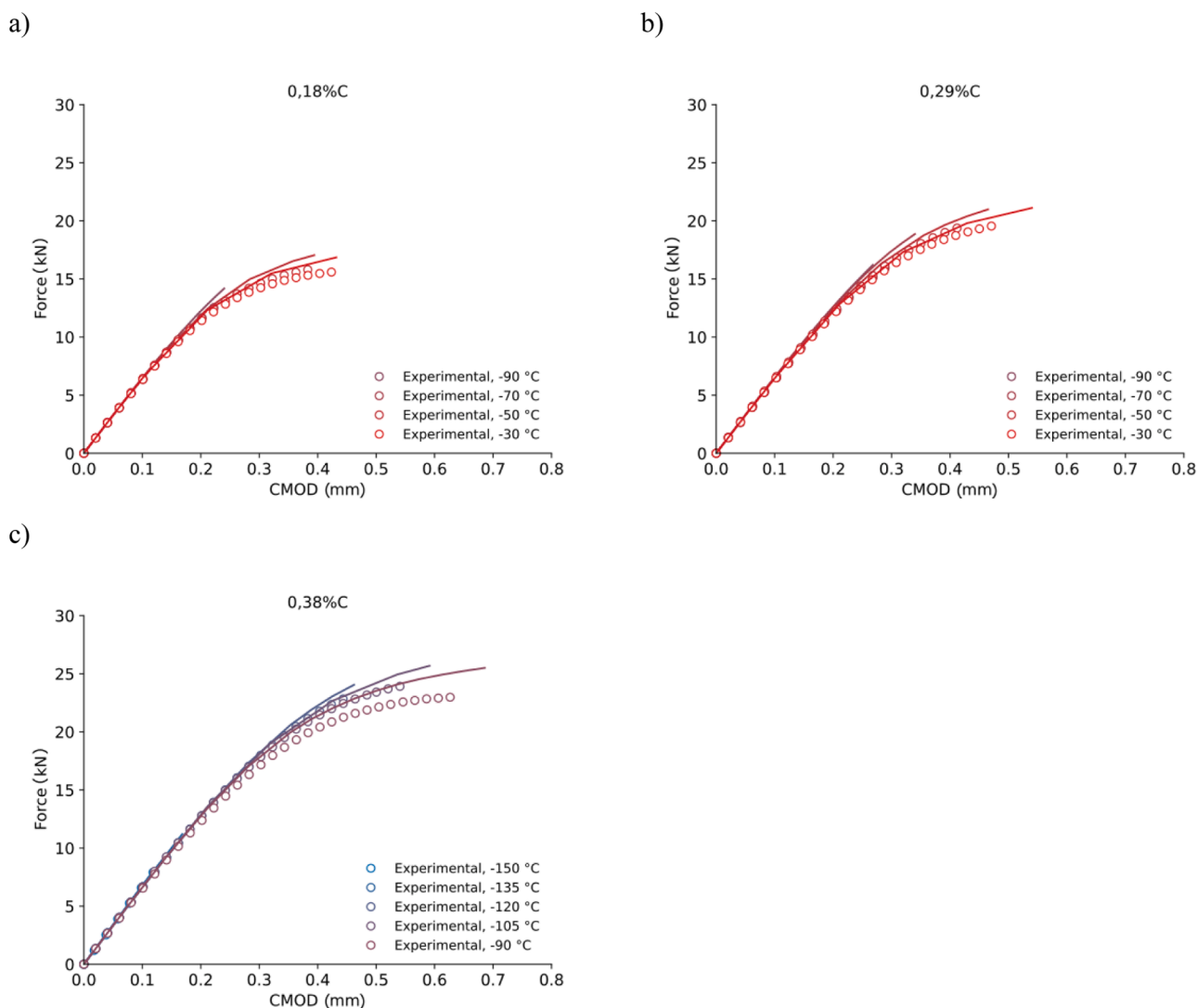


Fig. 15. Comparison between force vs CMOD simulated and experimental curves for (a) 0.18 %C, (b) 0.29 %C and (c) 0.38 %C materials.

stresses as the carbon content increases, leading to a potential detrimental effect;

- From a microstructural perspective, the reduction of the large carbide population [27,30–32], the reduction of ferritic grain size [27–29] and the evolution of the microstructure towards lower bainite/martensite [34] contribute to a strengthening against brittle failure. This trend is especially important at 0.38 %C since for this material the reduction of the ferritic grain size and the evolution towards lower bainite/martensite is significantly more pronounced than at 0.29 %C (Figs. 8 and Fig. 9).

Despite significant literature on the influence of microstructure on the brittle failure of low-alloyed steels, there is still no consensus on which microstructural parameter controls cleavage failure. This may be explained by the significant statistical correlation observed between different microstructural parameters. For instance, whilst grain size effects have been reported by several authors [48,49], it was also observed that there is a correlation between the size of the largest carbide and grain size in mild steels [50,51]. Bainitic packet sizes, prior austenitic grains sizes and cleavage facets sizes may also be correlated [30,52], making it difficult to isolate the effects of each microstructural parameter experimentally. One alternative to study the influence of each parameter independently is to use modelling strategies. For instance, Petch [49] proposed a model in which the critical cleavage stress

depends on both grain and carbide sizes. This model could be easily integrated into the available Microstructure Informed Brittle Fracture (MIBF) local approach model [8,9,53], which incorporates independently the effects of carbide population, local stresses/strains heterogeneous fields and also of the microstructural resistance. The results obtained from the resulting models can shed some light on the role of each microstructural parameter on the brittle failure of low-alloyed steels but demand additional studies.

In the present work, the influence of microsegregation was minimized due to the homogenisation heat treatment, which isolated the effect of the bulk chemical composition. Local microsegregation is often observed in macrosegregated industrial components and leads to the formation of a complex microstructure, composed of zones with different microstructural and mechanical properties. The unexpected evolution of transition temperature observed in the present work suggests that these microsegregated zones may play an important role in the embrittlement of RPV steels. This interpretation is consistent with the results observed by Yan and co-workers [10] for macrosegregated SA508 Gr.3, in which homogenization led to an increase of almost 60 J on the average absorbed energy due to the reduction of the M-A island's content for a nominal composition. However, it is important to note that some of the microstructural changes observed as carbon content increases in this work may not be representative of macrosegregation effects in large forgings. In a previous study with model materials

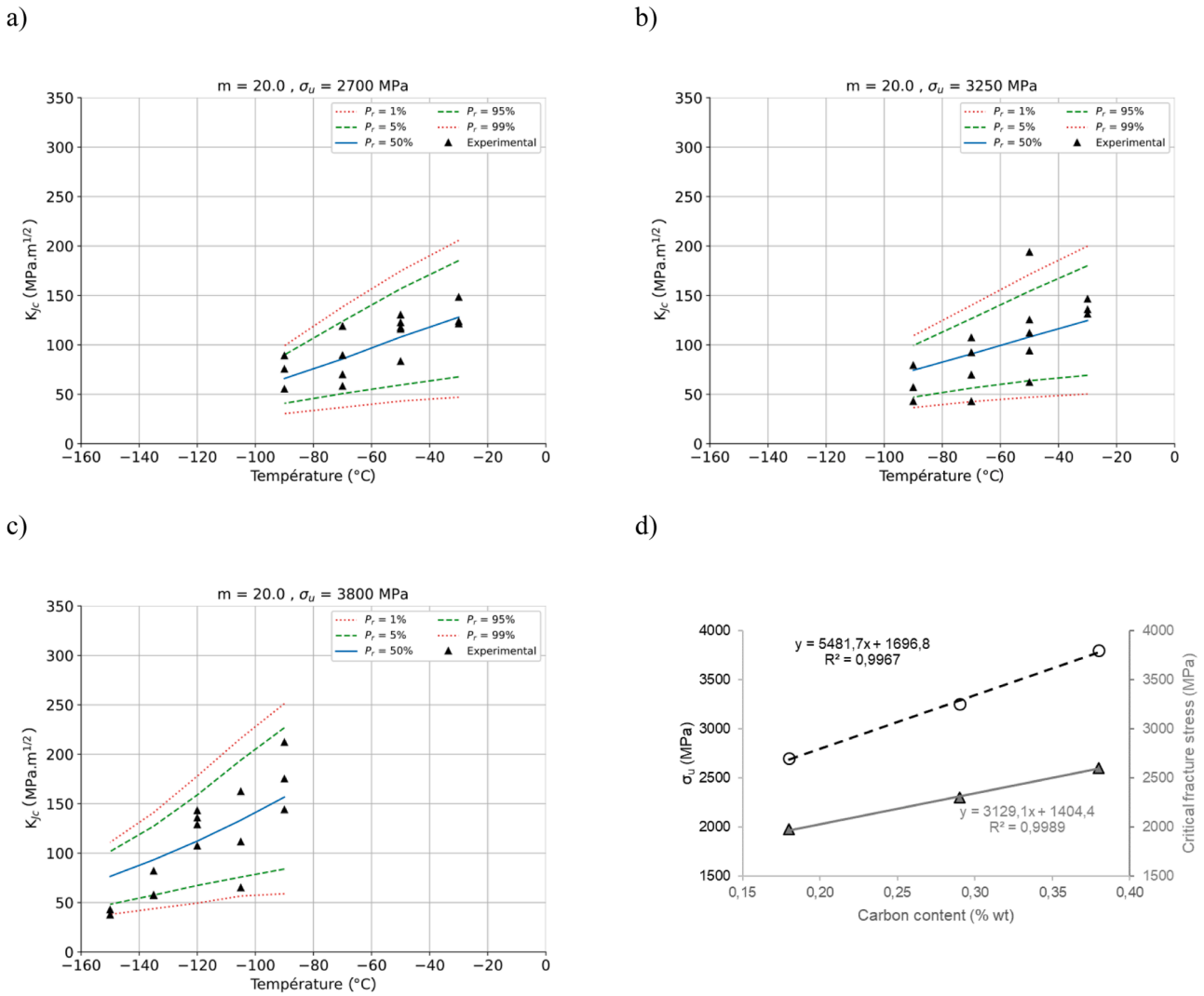


Fig. 16. Isoprobability curves at (a) 0.18 %C, (b) 0.29 %C, (c) 0.38 %C and (d) evolution of σ_u with carbon content in comparison with previously determined critical stress (Fig. 14d).

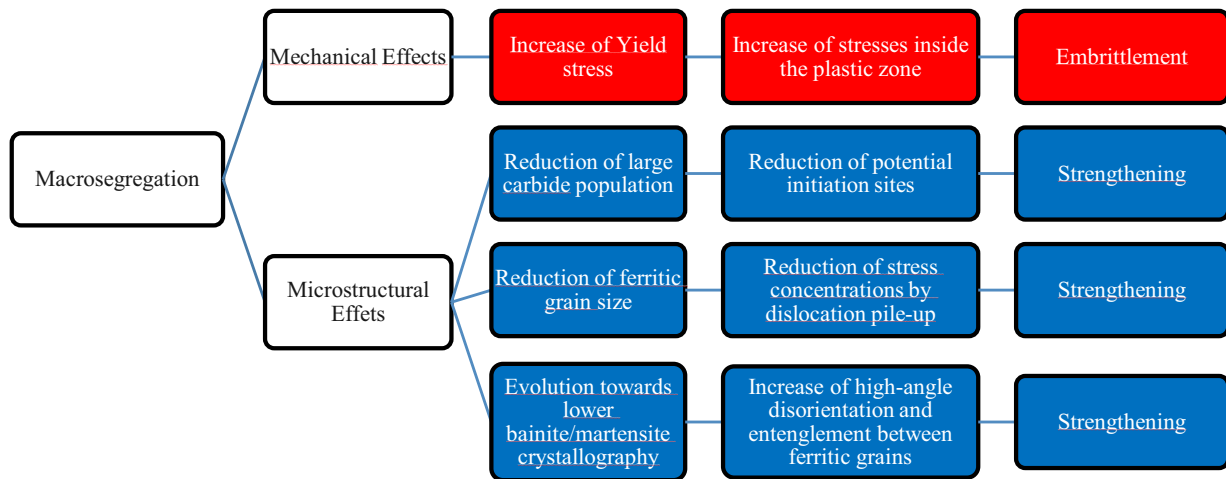


Fig. 17. Schematic representation of the effects associated with carbon content variation in this study.

containing microsegregations, no significant decrease of bainite grain size was seen between $\sim 0.18\%C$ and $\sim 0.38\%C$ [8,9]. In another study with specimens extracted from a macrosegregated large forging, no

significant differences between packet sizes were seen and the equivalent diameter of carbides increased slightly with carbon content [7], contrary to what is observed in our present study. Further studies are

necessary to elucidate the role of microsegregated zones on the brittle failure of RPV steels.

6. Conclusions

In the present work, the influence of a chemical composition evolution equivalent to the one found in macrosegregations on the brittle fracture mechanisms of RPV steel model alloys was investigated. Three model materials, submitted to a homogenization treatment prior to forging operations and post-forging heat treatments, were studied through mechanical tests, fractographic and microstructural analyses, and modelling using the local approach to fracture. The first one with a chemical composition similar to the 18MND5 RPV steel ($\sim 0.18\%$ C, close to ASME A508 Gr3 Cl2) and the other two materials with chemical compositions simulating zones of large ($\sim 0.29\%$ C) and intense ($\sim 0.38\%$ C) positive macrosegregation. Based on the aforementioned results, the following conclusions can be drawn:

- 1) As expected, yield stress increased and upper shelf energy decreased as the carbon content increased. However, the lowest transition temperatures T_0 and T_{56J} were unexpectedly observed for the 0.38 % C alloy, whilst comparable temperatures were observed for 0.18 % C and 0.29 % C;
- 2) Brittle fracture mechanism depends on the carbon content: cleavage was observed at 0.18 % C and 0.29 % C, and both cleavage and intergranular fracture were present at 0.38 % C. The presence of intergranular fracture at 0.38 % C is explained by the substantial increase in transgranular cleavage resistance and not by grain boundary embrittlement since the mass content of impurity elements is very limited in this model alloys, and it exhibits good toughness properties;
- 3) At 0.18 and 0.29 % C, cleavage fracture initiated mainly at Molybdenum/Manganese-enriched carbides located near or on cleavage facet boundaries, which are believed to be prior austenitic grain boundaries. The equivalent diameter of carbides identified at initiation sites ranged from 0.20 to 0.80 μm ;
- 4) The carbon content variation is associated with four microstructural effects: increase in total carbide volume fraction, reduction of fraction of large carbides ($>0.20\ \mu\text{m}$), reduction of ferritic grain size and evolution towards lower bainite/martensite;
- 5) Yield stress probably increases with the carbon content due to the reduction of the ferritic grain size and increase in the carbide volume fraction;
- 6) The combination of the reduction of the fraction of large carbides, reduction of ferritic grain size and evolution towards lower bainite/martensite leads to an increase in the resistance against purely brittle failure. This is confirmed by the increase of the critical fracture stress estimated from Charpy tests;
- 7) The cleavage resistance microstructural parameter σ_{us} , equivalent to the (σ_u, m) parameters of the Beremin model evolves with carbon content, following the same trend as the one observed for the critical

fracture stress estimated from Charpy tests. This confirms that the evolution of the microstructure plays an important role in the evolution of transition temperatures;

- 8) The unusual evolution of the reference temperature T_0 can be explained by the competition between the embrittlement due to the increase of the yield stress on one side and the strengthening due to the reduction of the large carbide fraction, reduction of ferritic grain size and evolution towards highly disorientated and entangled lower bainite/martensite microstructures on the other side. In the present study, for the material with 0.29 % C and particularly for the material with 0.38 % C, these strengthening effects were strong enough to outweigh the embrittlement effect associated with yield strength increase.

Note that the present analyses and conclusions are drawn from the results obtained on well homogenized model materials, with the objective to isolate and characterize the chemical composition effect without the influence of micro-segregation. Any attempt to extend the present observations and conclusions to the macroscopic behaviour of macrosegregated industrial components would also require a better understanding of the effect of macro-segregation on the localized micro-segregations and on the resulting microstructures, as they can be observed in some industrial materials.

CRedit authorship contribution statement

Cainã Bemfica: Writing – review & editing, Writing – original draft, Methodology, Investigation, Formal analysis. **Ludovic Vincent:** Writing – review & editing, Validation, Supervision, Project administration, Methodology, Investigation, Formal analysis. **Bernard Marini:** Writing – review & editing, Validation, Supervision, Project administration, Methodology, Investigation, Formal analysis. **Jean-Philippe Mathieu:** Writing – review & editing, Validation, Project administration, Funding acquisition, Data curation. **Daniel Brimbal:** Writing – review & editing, Validation, Project administration, Funding acquisition, Data curation.

Declaration of competing interest

The authors declare that they have no known competing financial interests or personal relationships that could have appeared to influence the work reported in this paper.

Acknowledgements

This work has been funded and scientifically supported by the CEA-EDF-Framatome R&D Institute (I3P). The authors specifically acknowledge Gaëlle Leopold from EDF and Elizabeth Deneuvillers from Framatome for the fabrication and mechanical characterization of the presented material. The authors would also like to thank A. Gangloff (CEA) for the help with EBSD, carbide and fractographic analyses and J-B. Delattre (CEA) for the fruitful discussions on the results.

Appendices

Tables A1 and A2.

Table A1
Summary of fractographic analyses carried out for Charpy specimens.

Specimen	C (%)	Temperature (°C)	Energy (J)	Initiation site	Distance from notch (mm)	Propagation mode
CV-NS-A7	0.18	−20	39.9	Carbide with Mo and Mn, $d = 0.27\ \mu\text{m}$	1.65	Cleavage
CV-NS-B4	0.18	−40	28.8	Possible carbide, $d = 0.20\ \mu\text{m}$	1.45	Cleavage
CV-MS-B9	0.29	−20	47.6	Possible grain boundary	1.20	Cleavage
CV-MS-B4	0.29	−40	25.7	Possible carbide, $d = 0.36\ \mu\text{m}$	1.27	Cleavage
CV-IS-B9	0.38	−40	57.0	Unidentified	-	Cleavage + Intergranular
CV-IS-A9	0.38	−60	37.8	Unidentified	-	Cleavage + Intergranular

Table A2

Summary of fractographic analyses carried out for CT specimens.

Specimen	C (%)	Temperature (°C)	Fracture toughness (MPa√m)	Initiation site	Distance from precrack tip (μm)	Propagation mode
CT-NS-B3	0.18	-70	90.4	Carbide with Mo and Mn, d = 0.80 μm	55	Cleavage
CT-NS-C4	0.18	-50	116.2	Possible grain boundary	128	Cleavage
CT-NS-A5	0.18	-30	147.6	Carbide with Mo and Mn, d = 0.72 μm	168	Cleavage
CT-MS-B5	0.29	-90	80	Close to rough facet	64	Cleavage
CT-MS-A4	0.29	-70	93	Carbide with Mo and Mn, d > 0.68 μm	57	Cleavage
CT-MS-C2	0.29	-50	112	Carbide with Mo and Mn, d = 0.54 μm	79	Cleavage
CT-MS-B4	0.29	-30	146	Carbide with Mo and Mn, d = 0.67 μm	145	Cleavage
CT-IS-B5	0.38	-135	83.1	Unidentified	-	Cleavage + Intergranular
CT-IS-C1	0.38	-120	107.9	Unidentified	-	Cleavage + Intergranular
CT-IS-C3	0.38	-105	111.9	Unidentified	-	Cleavage + Intergranular
CT-IS-A4	0.38	-90	173.9	Unidentified	-	Cleavage + Intergranular

Data availability

The authors do not have permission to share data.

References

- S. Sallet, N. Rupa, C. Benhamou, Impact of large forging macrosegregations on the reactor pressure vessel surveillance program. Fontevraud (France), SFEN, 2006.
- K. Shi, Y. Zhang, Y. Yang, B. Zheng, H. Xie, S. Gao, X. Bai, X. Fu, X. Shao, Fracture failure analysis of steam generator channel heads with high carbon macro-segregation, Eng. Fail. Anal. 113 (2020) 104540, <https://doi.org/10.1016/j.engfailanal.2020.104540>.
- E.J. Pickering, H. Bhadeshia, The consequences of macroscopic segregation on the transformation behavior of a pressure-vessel steel, J. Pressure Vessel Technol.-Transact. ASME 136 (2014) 031403, <https://doi.org/10.1115/1.4026448>.
- H. Liu, H. Zhang, The influence of carbon content and cooling rate on the toughness of Mn-Mo-Ni low-alloy steels. HSLA Steels 2015, Microalloying 2015 & Offshore Engineering Steels, 2015, pp. 247–252, <https://doi.org/10.1002/9781119223399.ch25>, 2015.
- A. Lefrançois, T. Berger, B. Lefever, S. Marie, FA3 RPV carbon segregation issue: representativeness and transferability of sacrificial parts, in: D. Piping (Ed.), ASME Pressure Vessels and Piping Conference (PVP 2018), Prague, Czech Republic, 2018.
- S. Marie, J. Demarecaux, P. Fichot, M. Hajjaj, C. Miller, Flamanville EPR RPV's heads carbon segregation: impact of the high carbon segregation on the mechanical properties of the RPV steel, in: PVP2018, Volume 6A: Materials and Fabrication, 2018. <https://doi.org/10.1115/PVP2018-84330>.
- S. Cazottes, C. Dessolin, D. Fabrègue, S. Curelea, D. Brimbal, F. Roch, X. Boulnat, Quantitative microstructural characterization of nuclear grade bainitic steel: influence of macrosegregations in full-scale forgings, Mater. Charact. 176 (2021) 111098, <https://doi.org/10.1016/j.matchar.2021.111098>.
- S. Ren, B. Marini, P. Joly, P. Todeschini, Microstructure-informed modelling of the fracture toughness of alloys representing macro-segregated zones in heavy forgings, Procedia Struct. Integr. 28 (2020) 684–692, <https://doi.org/10.1016/j.prostr.2020.10.079>.
- S.C. Ren, B. Marini, P. Forget, Modelling the effect of macro-segregation on the fracture toughness of heavy forgings using FFT based crystal plasticity simulations, Eng. Fract. Mech. 272 (2022) 108694, <https://doi.org/10.1016/j.engfracmech.2022.108694>.
- G. Yan, L. Han, C. Li, X. Luo, J. Gu, Effect of macrosegregation on the microstructure and mechanical properties of a pressure-vessel steel, Metall. Mater. Trans. A 48 (2017) 3470–3481, <https://doi.org/10.1007/s11661-017-4119-5>.
- Y.-R. Im, B.-J. Lee, Y.J. Oh, J.H. Hong, H.-C. Lee, Effect of microstructure on the cleavage fracture strength of low carbon Mn–Ni–Mo bainitic steels, J. Nucl. Mater. 324 (2004) 33–40, <https://doi.org/10.1016/j.jnucmat.2003.09.003>.
- L. Oger, S. Vernier, P. Joly, J.-M. Cloue, L. Laffont, E. Andrieu, Study of the relationships between microstructure and local mechanical properties in the ductile-to-brittle transition of a bainitic steel containing local segregations, Mater. Today Commun. 37 (2023) 107436, <https://doi.org/10.1016/j.mtcomm.2023.107436>.
- A.-F. Gourgue, H.M. Flower, T.C. Lindley, Electron backscattering diffraction study of acicular ferrite, bainite, and martensite steel microstructures, Mater. Sci. Technol. 16 (2000) 26–40, <https://doi.org/10.1179/026708300773002636>.
- S. Zajac, V. Schwinn, K.H. Tacke, Characterisation and quantification of complex bainitic microstructures in high and ultra-high strength linepipe steels, Mater. Sci. Forum 500 (501) (2005) 387–394, <https://doi.org/10.4028/www.scientific.net/MSF.500-501.387>.
- D.G. Brandon, The structure of high-angle grain boundaries, Acta Metall. 14 (1966) 1479–1484, [https://doi.org/10.1016/0001-6160\(66\)90168-4](https://doi.org/10.1016/0001-6160(66)90168-4).
- F.M. Beremin, A. Pineau, F. Mudry, J.-C. Devaux, Y. D'Escatha, P. Ledermann, A local criterion for cleavage fracture of a nuclear pressure vessel steel, Metall. Trans. A 14 (1983) 2277–2287, <https://doi.org/10.1007/BF02663302>.
- A. Martin-Meizoso, I. Ocana-Arizarcorreta, J. Gil-Sevillano, M. Fuentes-Pérez, Modelling cleavage fracture of bainitic steels, Acta Metall. Mater. 42 (1994) 2057–2068, [https://doi.org/10.1016/0956-7151\(94\)90031-0](https://doi.org/10.1016/0956-7151(94)90031-0).
- G.T. Hahn, The influence of microstructure on brittle fracture toughness, Metall. Trans. A 15 (1984) 947–959, <https://doi.org/10.1007/BF02644685>.
- P. Chekhonin, A. Das, F. Bergner, E. Altstadt, Microstructural characterisation of brittle fracture initiation sites in reactor pressure vessel steels, Nuclear Mater. Energy 37 (2023) 101511, <https://doi.org/10.1016/j.nme.2023.101511>.
- C. Li, L. Han, G. Yan, Q. Liu, X. Luo, J. Gu, Time-dependent temper embrittlement of reactor pressure vessel steel: correlation between microstructural evolution and mechanical properties during tempering at 650 °C, J. Nucl. Mater. 480 (2016) 344–354, <https://doi.org/10.1016/j.jnucmat.2016.08.039>.
- J.P. Naylor, M. Guttman, Mechanism of upper-nose temper embrittlement in Mn–Ni–Mo A533 gr. B steel, Metall. Sci. 15 (1981) 433–441, <https://doi.org/10.1179/msc.1981.15.10.433>.
- X.Z. Zhang, J.F. Knott, Cleavage fracture in bainitic and martensitic microstructures, Acta Mater. 47 (1999) 3483–3495, [https://doi.org/10.1016/S1359-6454\(99\)00200-1](https://doi.org/10.1016/S1359-6454(99)00200-1).
- J.-B. Delattre, Étude Du Lien Entre Traitement Thermique, Propriétés Mécaniques Et Armage De La Rupture Fragile Par Clivage D'un Acier Faiblement Allié Tempéré Revenu, Thèse de Doctorat, Ecole des Mines de Paris, 2023.
- S. Lee, S. Kim, B. Hwang, B.S. Lee, C.G. Lee, Effect of carbide distribution on the fracture toughness in the transition temperature region of an SA 508 steel, Acta Mater. 50 (2002) 4755–4762, [https://doi.org/10.1016/S1359-6454\(02\)00313-0](https://doi.org/10.1016/S1359-6454(02)00313-0).
- E O Hall, The deformation and ageing of mild steel: III discussion of results, Proc. Phys. Soc. London Sect. B 64 (1951) 747, <https://doi.org/10.1088/0370-1301/64/9/303>.
- N.J. Petch, The cleavage strength of polycrystals, J. Iron and Steel Instit. 174 (1953) 25–28.
- K.-H. Lee, S. Park, M.-C. Kim, B.-S. Lee, D.-M. Wee, Characterization of transition behavior in SA508 gr.4N Ni–Cr–Mo low alloy steels with microstructural alteration by Ni and Cr contents, Mater. Sci. Eng.: A 529 (2011) 156–163, <https://doi.org/10.1016/j.msea.2011.09.012>.
- A. Echeverria, J.M. Rodriguez-Ibabe, The role of grain size in brittle particle induced fracture of steels, Mater. Sci. Eng.: A 346 (2003) 149–158, [https://doi.org/10.1016/S0921-5093\(02\)00538-5](https://doi.org/10.1016/S0921-5093(02)00538-5).
- J.R. Tarpani, W.W. Bose Filho, D. Spinelli, Grain size effects in the quasi-static fracture resistance of a thermally embrittled RPV steel (annealed microstructures), J. Mater. Eng. Perform. 11 (2002) 414–421, <https://doi.org/10.1361/105994902770343944>.
- K.-H. Lee, M.-C. Kim, W.-J. Yang, B.-S. Lee, Evaluation of microstructural parameters controlling cleavage fracture toughness in Mn–Mo–Ni low alloy steels, Mater. Sci. Eng.: A 565 (2013) 158–164, <https://doi.org/10.1016/j.msea.2012.12.024>.
- W.-J. Yang, B.-S. Lee, Y.-J. Oh, M.-Y. Huh, J.-H. Hong, Microstructural parameters governing cleavage fracture behaviors in the ductile–brittle transition region in reactor pressure vessel steels, Mater. Sci. Eng.: A 379 (2004) 17–26, <https://doi.org/10.1016/j.msea.2003.10.289>.
- P. Bowen, S.G. Druce, J.F. Knott, Effects of microstructure on cleavage fracture in pressure vessel steel, Acta Metall. 34 (1986) 1121–1131, [https://doi.org/10.1016/0001-6160\(86\)90222-1](https://doi.org/10.1016/0001-6160(86)90222-1).
- A. Benarosch, B. Marini, C. Toffolon-Maslet, Z. Trzaska, E. Meslin, I. Guillot, Effect of cooling rate on the microstructures of three low carbon alloys with different

- manganese and molybdenum contents, *Metallurg. Res. Technol.* 119 (2022) 520, <https://doi.org/10.1051/metal/2022059>.
- [34] B. Marini, X. Averty, P. Wident, P. Forget, F. Barcelo, Effect of the bainitic and martensitic microstructures on the hardening and embrittlement under neutron irradiation of a reactor pressure vessel steel, *J. Nucl. Mater.* 465 (2015) 20–27, <https://doi.org/10.1016/j.jnucmat.2015.05.023>.
- [35] R. Chaouadi, A. Fabry, On the utilization of the instrumented Charpy impact test for characterizing the flow and fracture behavior of reactor pressure vessel steels, in: D. Francois, A. Pineau (Eds.), *From Charpy to Present Impact Testing*, European Structural Integrity Society, 2002, pp. 103–117.
- [36] A. Andrieu, A. Pineau, J. Besson, D. Ryckelynck, O. Bouaziz, Beremin model: methodology and application to the prediction of the Euro toughness data set, *Eng. Fract. Mech.* 95 (2012) 102–117, <https://doi.org/10.1016/j.engfracmech.2011.10.019>.
- [37] C. Ruggieri, A modified local approach including plastic strain effects to predict cleavage fracture toughness from subsized precracked Charpy specimens, *Theor. Appl. Fract. Mech.* 105 (2020) 102421, <https://doi.org/10.1016/j.tafmec.2019.102421>.
- [38] J.W. Hutchinson, Singular behaviour at the end of a tensile crack in a hardening material, *J. Mech. Phys. Solids* 16 (1968) 13–31, [https://doi.org/10.1016/0022-5096\(68\)90014-8](https://doi.org/10.1016/0022-5096(68)90014-8).
- [39] J.R. Rice, G.F. Rosengren, Plane strain deformation near a crack tip in a power-law hardening material, *J. Mech. Phys. Solids* 16 (1968) 1–12, [https://doi.org/10.1016/0022-5096\(68\)90013-6](https://doi.org/10.1016/0022-5096(68)90013-6).
- [40] M. Umemoto, Z.G. Liu, K. Masuyama, K. Tsuchiya, Influence of alloy additions on production and properties of bulk cementite, *Scr. Mater.* 45 (2001) 391–397, [https://doi.org/10.1016/S1359-6462\(01\)01016-8](https://doi.org/10.1016/S1359-6462(01)01016-8).
- [41] M. Umemoto, H. Ohtsuka, Mechanical properties of cementite, *ISIJ Int.* 62 (2022) 1313–1333, <https://doi.org/10.2355/isijinternational.ISIJINT-2022-048>.
- [42] Y. Liu, Y. Jiang, J. Xing, R. Zhou, J. Feng, Mechanical properties and electronic structures of M23C6 (M = Fe, Cr, Mn)-type multicomponent carbides, *J. Alloys Compd.* 648 (2015) 874–880, <https://doi.org/10.1016/j.jallcom.2015.07.048>.
- [43] N. Osipov, A.F. Gourgues-Lorenzon, B. Marini, V. Mounoury, F. Nguyen, G. Cailletaud, FE modelling of bainitic steels using crystal plasticity, *Philos. Mag.* 88 (2008) 3757–3777, <https://doi.org/10.1080/14786430802566380>.
- [44] S. Raoul, B. Marini, A. Pineau, Effect of microstructure on the susceptibility of a 533 steel to temper embrittlement, *J. Nucl. Mater.* 257 (1998) 199–205, [https://doi.org/10.1016/S0022-3115\(98\)00467-X](https://doi.org/10.1016/S0022-3115(98)00467-X).
- [45] C. Naudin, J.M. Frund, A. Pineau, Intergranular fracture stress and phosphorus grain boundary segregation of a Mn-Ni-Mo steel, *Scr. Mater.* 40 (1999) 1013–1019, [https://doi.org/10.1016/S1359-6462\(99\)00069-X](https://doi.org/10.1016/S1359-6462(99)00069-X).
- [46] J. Kameda, Y. Nishiyama, Combined effects of phosphorus segregation and partial intergranular fracture on the ductile–brittle transition temperature in structural alloy steels, *Mater. Sci. Eng.: A* 528 (2011) 3705–3713, <https://doi.org/10.1016/j.msea.2011.01.018>.
- [47] K. Wang, Y. Guo, S. Song, Quantitative dependence of ductile-to-brittle transition on phosphorus grain boundary segregation for a novel Ni–Cr–Mo RPV steel, *J. Mater. Res. Technol.* 15 (2021) 6404–6414, <https://doi.org/10.1016/j.jmrt.2021.11.092>.
- [48] P. Brozzo, G. Buzzichelli, A. Mascanzoni, M. Mirabile, Microstructure and cleavage resistance of low-carbon bainitic steels, *Metal. Sci.* 11 (1977) 123–130, <https://doi.org/10.1179/msc.1977.11.4.123>.
- [49] N.J. Petch, The influence of grain boundary carbide and grain size on the cleavage strength and impact transition temperature of steel, *Acta Metall.* 34 (1986) 1387–1393, [https://doi.org/10.1016/0001-6160\(86\)90026-X](https://doi.org/10.1016/0001-6160(86)90026-X).
- [50] D.A. Curry, J.F. Knott, Effects of microstructure on cleavage fracture stress in steel, *Metal. Sci.* 12 (1978) 511–514, <https://doi.org/10.1179/msc.1978.12.11.511>.
- [51] S. Kim, S. Lee, B.S. Lee, Effects of grain size on fracture toughness in transition temperature region of Mn–Mo–Ni low-alloy steels, *Mater. Sci. Eng.: A* 359 (2003) 198–209, [https://doi.org/10.1016/S0921-5093\(03\)00344-7](https://doi.org/10.1016/S0921-5093(03)00344-7).
- [52] L. Rancel, M. Gómez, S.F. Medina, I. Gutierrez, Measurement of bainite packet size and its influence on cleavage fracture in a medium carbon bainitic steel, *Mater. Sci. Eng.: A* 530 (2011) 21–27, <https://doi.org/10.1016/j.msea.2011.09.001>.
- [53] P. Forget, B. Marini, L. Vincent, Application of local approach to fracture of an RPV steel: effect of the crystal plasticity on the critical carbide size, *Procedia Struct. Integr.* 2 (2016) 1660–1667, <https://doi.org/10.1016/j.prostr.2016.06.210>.